A coupled Volume of Fluid -Phase Field method for direct numerical simulation of insoluble surfactant-laden interfacial flows and application to rising bubbles

Palas Kumar Farsoiya, Stéphane Popinet, Howard A Stone, Luc Deike

A coupled Volume of Fluid Phase Field method for direct numerical simulation of insoluble surfactant-laden interfacial flows and application to rising bubbles

Palas Kumar Farsoiya[1,2], Stéphane Popinet [3], Howard A. Stone[2], and Luc Deike [2,4*]
[1] *Department of Chemical Engineering, Indian Institute of Technology Roorkee, Roorkee, Uttarakhand 247667, India*
[2] *Department of Mechanical and Aerospace Engineering, Princeton University, Princeton, New Jersey 08544, USA*
[3] *Sorbonne Université, CNRS, UMR 7190, Institut Jean le Rond ∂'Alembert, F-75005 Paris, France*
[4] *High Meadows Environmental Institute, Princeton University, Princeton, New Jersey 08544, USA*

Improved numerical methods are needed to understand the effect of surfactants in interfacial fluid mechanics, with various applications including thin films, inkjet printing and ocean-atmosphere interactions. We provide a three-dimensional coupled Volume of Fluid (VoF) and Phase Field numerical approach to simulate the effects of insoluble surfactant-laden flows. The framework is validated against analytical cases for surfactant transport and Marangoni stresses. We then systematically investigate a single surfactant-laden rising bubble. The characteristics of a clean bubble rising in a quiescent liquid are governed by non-dimensional numbers, i.e., the Galileo number Ga, which compares inertial and viscous effects, and the Bond number Bo, which compares gravitational and surface tension stresses. The effect of insoluble surfactants introduces an additional independent parameter, the Marangoni number Ma, comparing the change in surface tension forces due to gradients in surfactants concentration with viscous forces. We apply our numerical methods to investigate the influence of surfactants (through the Marangoni number) on rising bubbles in otherwise quiescent fluids. We observe that an increase in the Marangoni number first decreases the rise velocity before reaching a limiting value at high Ma. The value of Ma necessary to observe a significant slowdown increases with Ga. We discuss the associated surfactant accumulation and the vortical dynamics when a steady state is reached. Finally, we perform three-dimensional simulations and demonstrate that Marangoni effects can induce a change in the rise trajectory from spiraling to zigzagging for set values of Bo and Ga, consistent with experimental results.

I. INTRODUCTION

A. General context

Surfactants – a contraction of the term **surf**ace-**act**ive age**nts** – are found in a broad range of applications owing to their ability to lower surface tension and facilitate interactions between different phases. Surfactants are found in everyday products, as they are essential components in detergents and cleaning agents, enabling emulsification and removal of oils and dirt from surfaces. For example, surfactants are widely used in personal care items and cosmetics as they contribute to foaming and emulsification properties, while in pharmaceuticals they aid in drug delivery and solubilization. Also, surfactants play key roles in agriculture as adjuvants in pesticide formulations, and in the oil and gas industry they are used for enhanced oil recovery. They find application in paints, coatings, textiles, and even firefighting foams. Additionally, surfactants are integral to biomedical applications and environmental remediation, which further illustrates their versatile and indispensable use across diverse sectors [1, 2].

Air-liquid interfaces are ubiquitous in both nature and industry [3–5]. Their manifestations range from rising air bubbles in water, rain droplets, sloshing in tanks, and breaking waves in the ocean to fuel injection and sprays. Precise characterization of surfactant effects on interfacial processes is an active area of research. Examples of recent studies include effects such as delayed coalescence of droplets with differing surface tensions [6] and how surfactants hinder the breakup of droplets during inkjet printing, thus averting the formation of satellite droplets [7]. Separately, bubbles forming on a liquid surface coalesce more at low surfactant concentrations and less at high concentrations [8], while also affecting mass transfer at the ocean-atmosphere interface [9]. Spray generation from bursting bubbles shows non-monotonic behavior as the surfactant concentration is increased [10], which affects the generation of jet drops [11] as well as film drops [12]. While surfactants effects are known to be important at the scale of the capillary length (typically mm to cm), the dynamics induced by Marangoni stresses due to surfactant gradients can affect large-scale phenomena such as waves, as demonstrated by laboratory experiments on spilling breakers [13–15] and plunging breakers [16]. A historical exposition by Lohse [17] delves into the impact of surfactants on waves, tracing

* ldeike@princeton.edu

a timeline from the seminal observation by Franklin and Brownrigg [18] of smooth wakes from ships that release oil to Pockels' experiments [19] designed to measure surface tension. The wide range of applications and complexity of processes motivate the development of versatile numerical methods to accurately quantify the influence of surfactants on interfacial fluid dynamics.

B. Surfactants effect on bubbles

Manikantan and Squires [20] discuss how surfactants can introduce hidden variables that control fluid flows and have effects that are still not well understood, and review classic problems such as bubbles rising in quiescent liquids. Interfaces with high surface tension like air/water, liquid metals/air, and aqueous liquids/non-polar liquids are especially susceptible to significant interfacial effects even for trace amounts of surface-active contaminants (contaminants hereafter). In the context of bubbles and drops, the theoretical analyses started by Frumkin [21] and Levich [22] to investigate contaminant effects assume low-Reynolds-number flow and soluble surfactants. Experiments by Savic [23] on insoluble surfactant-laden rising bubbles observed an increased drag with contamination.

The increased drag can be explained through a stagnant cap model: surfactants are collected at the back of the bubble, causing a surface tension gradient localized at the cap boundary where the contaminated part meets the clean parts of the interface. Hence, the Marangoni stress is tangentially directed towards the top of the bubble. This stress opposes the motion of the fluid and creates a zone where the tangential velocity vanishes and an immobile interface is formed, i.e., a stagnant cap. The initial studies provided analytical descriptions [23–25]. For a foundational understanding of the motion of surface-active bubbles and drops, Harper [26] offers an early comprehensive literature survey and theoretical analysis.

Complementary to the experimental and theoretical investigations, there have been a wide range of numerical studies, with different methods, as summarized in Table 1; these papers include discussion of various physical effects of surfactants on bubble dynamics. There is a rich literature of axisymmetric and three-dimensional simulations of various limiting cases [27, 28] as well as direct numerical simulations (DNS, solving the Navier-Stokes equations), for both insoluble and soluble surfactants effects on rising bubbles [29–31], bubble lifetime [32], bursting bubbles [33], among others. However, a numerical investigation quantifying the effect of insoluble surfactants on a rising unconfined bubble, including three-dimensional configurations with large bubble deformations and unstable paths, has not been systematically performed.

C. The need for a versatile numerical framework

The experimental studies provide a picture of coupled interfacial phenomena with Marangoni effects. Interfacial fluid mechanics problems with surfactants are also dependent on initial conditions (such as deposition) that are sometimes difficult to control in experiments. The surfactant concentration on interfaces is difficult to measure and generally experimental data is provided in terms of the bulk concentration of surfactants. Tracking how much surfactant is adsorbed at the interface is challenging.

Numerical simulations can provide a comprehensive picture of surfactant transport and distribution, and its effect on hydrodynamics, as a result of the ability to control initial conditions and determine all flow field data. Also, numerical simulations provide the opportunity to switch on and off some effects, such as adsorption-desorption, to change from a soluble to an insoluble surfactant or include a thermal gradient.

There are many numerical studies and methods considering Marangoni effects due to thermal gradients, e.g., [34–37]. However, in the presence of surfactants, the Marangoni effects need to be coupled with surfactant transport on the interface. Transporting surfactants on a moving interface has been challenging in Eulerian numerical frameworks and is the focus of the present work.

Recent efforts have investigated how to simulate surfactant-laden flows using different approaches, which we summarize in Table I. The different representations of interfaces provide access to different kinds of physical problems that can be investigated, such as drop breakup in linear flows, rising bubbles, capillary waves, etc., which have been approached with boundary integral representations [38–40], Front-Tracking approaches [31, 41–45], Level-Set methods [29, 46–49], free energy and diffuse interface methods [50–54], Arbitrary Lagrangian-Eulerian (ALE) [55, 56] and algebraic Volume of Fluid (VoF) interface tracking methods [30, 57] for soluble surfactant-laden situations, as well as hybrid approaches coupling Level-Set and Front-Tracking [58, 59] and algebraic VoF coupled with a phase field [60].

The Volume of Fluid (VoF) method for interface tracking provides a mass-conserving approach for the numerical solution of two-phase Navier-Stokes equations. Such a numerical framework has been extended using the continuum surface stress method to include surfactants effects with a linear equation of state, i.e., the relationship between surface tension and surfactant concentration [62]. The surfactant transport is achieved by advecting a scalar between two layers

Interface Tracking	**Dimensions**	**Mesh**	**Citations**	Statement of Open-Source
Boundary Element	2D	Structured uniform mesh	Stone and Leal [38]	
	3D	Structured uniform mesh	Li and Pozrikidis [39], Feigl *et al.* [61]	
	3D	Unstructured mesh	Yon and Pozrikidis [40]	
Front-Tracking	2D	Structured uniform mesh for velocity/pressure, Unstructured for interface tracking	Muradoglu and Tryggvason [42]	
	3D	Structured uniform mesh for velocity/pressure, Unstructured for interface tracking	Muradoglu and Tryggvason [31]	
	3D	Structured Adaptive Mesh Refinement (AMR) for velocity/pressure, Unstructured for interface tracking	De Jesus *et al.* [43]	
Level-Set and Front-Tracking	3D	Structured uniform for velocity/pressure, Unstructured for interface tracking	Shin *et al.* [59]	
Level-Set	3D	Structured uniform mesh	Xu *et al.* [47]	
	2D	Structured uniform	Lakshmanan and Ehrhard [48]	
	2D	Structured uniform mesh	Piedfert *et al.* [49]	
	2D	Structured uniform mesh	Atasi *et al.* [29]	
Arbitrary Lagrangian-Eulerian (ALE)	3D	Unstructured Adaptive Mesh Refinement	Dieter-Kissling *et al.* [55], Meijer *et al.* [56]	
Phase Field	2D & 3D	Structure Adaptive Mesh Refinement	Teigen *et al.* [52, 53], Soligo *et al.* [54]	
Algebraic VoF	2D & 3D	Unstructured Adaptive Mesh Refinement	Pesci *et al.* [30], Antritter *et al.* [57]	
Algebraic VoF Phase Field	3D	Structured uniform mesh	Cannon *et al.* [60]	
Geometric VoF	2D & 3D	Structured uniform mesh	Renardy *et al.* [62]	
	2D	Unstructured Adaptive Mesh Refinement(AMR)	James and Lowengrub [63]	
Geometric VoF Phase Field	**2D & 3D**	**Structured Adaptive Mesh Refinement (AMR)**	**Present-Study**	**Open Source (GPL)**

TABLE I. Summary of representative studies of numerical methods for surfactant-laden flows in interfacial fluid dynamics. All of these methods solve the surfactants transport equations coupled with Marangoni stresses and the two-phase Navier-Stokes equations, with different interface tracking and mesh structures. The present work proposes an open-source geometric VoF method coupled with a Phase Field representation.

of VoF-tracked interfaces. A VoF-based approach applied to surfactant-induced Marangoni flow (in axisymmetric geometry), supporting an arbitrary equation of state for surface tension, was then proposed [63]. However, the extension to three-dimensional, adaptive meshes, with efficient parallelization is complex.

In this context, there is a need for a geometric VoF-based method for three-dimensional two-phase flows, accounting for surfactant transport and Marangoni stresses. Such a method is well suited for free-surface flows where distinct phases are separated by a sharp interface [64] and would allow investigating problems involving interface reconnection, such as jet break-up and breaking waves [65–67]. Moreover, the use of adaptive mesh refinement is essential for resolving multiscale problems in multiphase flows [67, 68]. Making these methods available within an open-source framework is also desirable for the community.

In the present study, we address this need, by adapting a method developed by Jain [69] for an interface-confined scalar represented by a Phase Field and incorporate it within the geometric VoF framework Basilisk [64, 68]. The present numerical approach uses volume fractions to represent the interface and solve the momentum equations. The Phase Field is only used to transport the surfactants and is computed using a signed distance from the interface [70]. As a signed distance calculation based on volume fractions adds significant computational cost, we transport the Phase Field as described by [71] and recompute the signed distance at a suitable frequency. The Marangoni force is

implemented based on continuum surface force modeling proposed by Seric *et al.* [35] and improved by Tripathi and Sahu [36]. The framework is implemented in Basilisk (Popinet and collaborators [72]), which is an open-source code, with well-documented test cases, supports adaptive mesh refinement (AMR), is highly scalable, and can be applied to a wide range of interfacial fluid mechanics problems. Here, we illustrate our methods on the classic problem of the rising bubble in an otherwise quiescent fluid and investigate the role of surfactants and Marangoni stresses. We demonstrate the effect of insoluble surfactants on an axisymmetric and 3D bubble rising in a quiescent liquid and provide quantitative measurements and qualitative features for this complex problem.

D. Outline

Section II presents the numerical framework, the set of equations to be considered, the implementation of surfactant transport, Marangoni stresses, and several validation cases. Section III illustrates the use of the numerical framework on the problem of a rising bubble in a quiescent fluid in the presence of surfactants. We present an extensive parameter sweep for the axisymmetric configuration, demonstrating the slow down of the bubble due to Marangoni effects, and illustrate the 3D capabilities of the numerical approach by showing how Marangoni effects can induce a transition in the bubble dynamics from ellipsoidal to zigzag motion. Section IV presents conclusions and prospects.

II. NUMERICAL FRAMEWORK

A. The Navier-Stokes and surfactants transport equations

We solve the three-dimensional, incompressible, two-phase Navier-Stokes equations using the open-source solver Basilisk [68, 72, 73],

$$\rho\left(\frac{\partial \mathbf{u}}{\partial t}+\mathbf{u}\cdot\nabla\mathbf{u}\right)=-\nabla p+\nabla\cdot(\mu(\nabla\mathbf{u}+\nabla\mathbf{u}^T))+\gamma\kappa\mathbf{n}\delta_s+\delta_m\nabla_s\gamma \tag{1}$$

$$\nabla\cdot\mathbf{u}=0, \tag{2}$$

$$\frac{\partial \mathcal{T}}{\partial t}+\mathbf{u}\cdot\nabla\mathcal{T}=0, \tag{3}$$

where $\mathbf{u}$, p, μ, ρ, γ, κ, $\mathbf{n}$ and $\mathcal{T}$ are, respectively, the velocity, pressure, viscosity, density, surface tension, twice the mean curvature, unit normal to the interface, $\mathbf{n}=\nabla\mathcal{T}/|\nabla\mathcal{T}|$, and volume fraction fields. The delta functions used to locate the interface are computed as $\delta_s=|\nabla\mathcal{T}|$ [68], $\delta_m=A_i/V_c$ [36] where A_i and V_c are the area of the interface and volume of the cell respectively [36]. As written, (1) directly incorporates interfacial effects, including Marangoni stresses from the gradient in surface tension.

The Basilisk solver has been validated extensively for complex interfacial flows, without Marangoni forces, including drop and bubble break-up, waves, and bursting bubbles [65, 67, 74–79]. It uses the projection method to compute the velocity and pressure and the geometric VoF method for the evolution of the interface between two immiscible fluids [80]. The Piecewise Linear Interface Calculation (PLIC) geometric interface and flux reconstruction ensures a sharp representation of the interface [81]. The surface tension force is modeled by the Continuum Surface Force (CSF) model [82], and uses generalized height functions for curvature [68]. The surface gradient of interfacial tension in the last term in Eq. (1) is modeled as proposed by Seric *et al.* [35].

The time-dependent advective-diffusion equation for insoluble surfactants with surface concentration $\Gamma(\mathbf{x},t)$ along a deforming interface is given by (Scriven [83], Stone [84]),

$$\frac{\partial\Gamma}{\partial t}+\nabla_s\cdot(\Gamma\mathbf{u}_s)+\Gamma(\nabla_s\cdot\mathbf{n})(\mathbf{u}\cdot\mathbf{n})=D_s\nabla_s^2\Gamma, \tag{4}$$

where $\nabla_s=(\mathbf{I}-\mathbf{nn})\cdot\nabla$ is the surface gradient operator and D_s is the surfactant diffusivity along the interface.

Multiphase flows can be characterized by a set of non-dimensional numbers. In the case of significant viscous and capillary effects, we can use the Ohnesorge number, $\mathrm{Oh}\equiv\mu/\sqrt{\rho\sigma L}$, with L a characteristic length (for example the bubble/drop size or the film thickness) together with viscosity and density ratios between the two phases.

The introduction of surfactant transport and induced stresses leads to additional non-dimensional numbers. The interfacial surfactant transport on the interface can be characterized by the Péclet number $\mathrm{Pe}_s\equiv UL/D_s$, with U a characteristic velocity. The surface tension is altered by surfactants and is generally described by an equation of state

or isotherm [20]. A linear isotherm relates surface tension as a linear function of surfactant concentration,

$$\gamma(\mathbf{x},t) = \gamma_0 \left(1 - \beta \frac{\Gamma(\mathbf{x},t)}{\Gamma_0}\right), \tag{5}$$

where Γ_0 is the initial surface concentration and β is a non-dimensional number characterizing the strength of the surface tension variation with a change in surfactant concentration. Other isotherms can be used within the present numerical framework, and have been proposed to describe experimental results on surfactants tested in the laboratory, as summarised by Manikantan and Squires [20]. The effect of variable surface tension introduces another parameter, often called the Marangoni number. The Marangoni number compares the Marangoni stress ($\Delta\gamma/L$) and viscous stress ($\mu U/L$). Different definitions of the Marangoni numbers have been used, depending on the regimes of interest [20]. In the present study, we consider moderate to high inertial effects (or Reynolds number), equivalent to low Oh number regimes, where surfactant transport is dominated by advection, i.e., $\mathrm{Pe}_s \gg 1$. We define the Marangoni number through a characteristic velocity U as $\mathrm{Ma} = \beta\gamma_0/(U\mu)$.

B. Numerical implementation of surfactant transport and Marangoni stresses

We use an approach developed by Jain [69] for interface-confined scalars for diffuse interface/Phase Field methods, which was not coupled to a flow solver. For the transport of insoluble surfactants having volumetric concentration c, an advection-diffusion equation is solved,

$$\frac{\partial c}{\partial t} + \nabla\cdot(\mathbf{u}c) = \nabla\cdot\left[D_s\left\{\nabla c - \frac{2(0.5-\phi)\mathbf{n}c}{\epsilon}\right\}\right], \tag{6}$$

where $c = \Gamma\xi$ and $\xi = \phi(1-\phi)/\epsilon$. The second term in the parenthesis on the right-hand side is an anti-diffusion term that keeps the scalar c concentrated at the interface. The Phase Field ϕ is computed from the signed distance χ,

$$\phi = \frac{1}{2}\left(1 - \tanh\left\{\frac{\chi}{2\epsilon}\right\}\right), \tag{7}$$

where ϵ defines the thickness of the Phase Field ϕ and is kept at $0.75\Delta x_{\min}$ in the present study, where Δx_{min} is the smallest grid size. The signed distance χ is calculated from the volume fractions $\mathcal{T}$ by iterating over the Hamilton-Jacobi equation,

$$\frac{\partial\chi}{\partial\tau} + \mathrm{sign}(\chi_0)(|\nabla\chi| - 1) = 0, \tag{8}$$

$$\chi_0 = \chi(x,0), \tag{9}$$

where τ is a fictitious time and χ_0 the initial Level-Set field. The redistancing procedure is adapted from Limare *et al.* [70]; see also the method proposed by [85–87]. The volume fraction, signed distance, Phase Field, and concentration are illustrated in Fig. 1(a,b,c).

Maintaining the positivity of the scalar concentration c is a requirement that should be consistently met throughout the simulation. Jain and Mani [88] derived a criterion sufficient to maintain the positivity of the scalar concentration c at all times. The discretized Eq. (6) is constrained by the positivity criterion $\Delta x \leq 2D_s/(|u|_{max} + D_s/\epsilon)$, where Δx and $|u|_{max}$ are the grid size and maximum interfacial velocity, respectively. This criterion is, however, prohibitive even at moderate Péclet numbers $\mathrm{Pe}_s = |u|_{max}L/D_s$, where L is the characteristic length. In the present study, we verify that the magnitude of negative values remains at most four orders less than the maximum surfactant concentration for the grid-converged solutions. Moreover, the explicit time discretization of the surface diffusion equation constrains the timestep size as $\Delta t \leq (\Delta x)^2/2N_dD_s$, where N_d is the number of dimensions.

As an illustration, the computed fields $f(x)$ in one dimension x, where the interface is at $x = 0$ between fluid 1 and fluid 2, are shown in Fig. 1. The volume fraction field in an interfacial cell has a value $0 < \mathcal{T} < 1$ (shown as a black dot), with 0 and 1 assigned to the bulk phases. The field χ is the signed distance from the interface $f(x) = x$ line, shown in blue in Fig. 1, while the Phase Field ϕ varies according to $\tanh(\chi/(2\epsilon)))$ and the concentration field c varies as the hyperbolic secant squared, $\mathrm{sech}^2(\chi/(2\epsilon)))$ [69]. Computing the signed distance from VoF is an expensive step [70], especially at high resolutions and for three-dimensional flows. To reduce the computational cost we evaluate Eq. (7) at a suitable frequency and for intermediate steps we use an accurate conservative Phase Field/diffuse interface model (ACDI) proposed by [71],

$$\frac{\partial\phi}{\partial t} + \nabla\cdot(\mathbf{u}\phi) = \nabla\cdot\left\{\zeta\left\{\epsilon\nabla\phi - \frac{1}{4}\left[1 - \tanh^2\left(\frac{\psi}{2\epsilon}\right)\right]\frac{\nabla\psi}{|\nabla\psi|}\right\}\right\}, \tag{10}$$

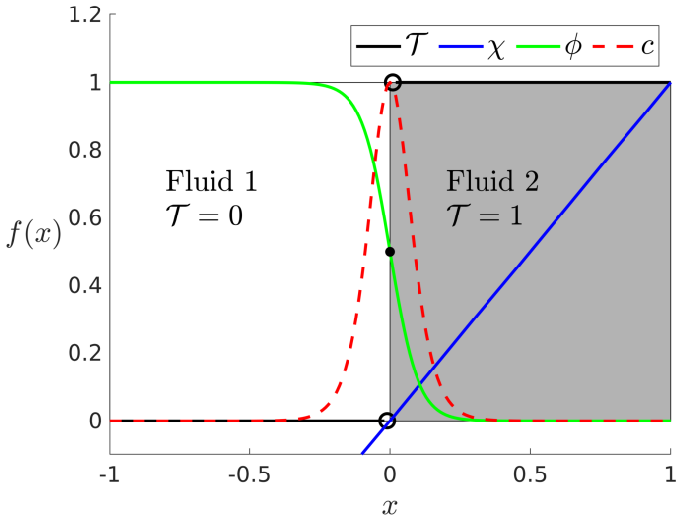

FIG. 1. Schematic representation of the VoF field $\mathcal{T}$, the signed-distance field χ, the Phase Field ϕ, and the volumetric surfactant concentration c. The momentum equations use the volume fraction $\mathcal{T}$ to compute the fluid properties. The transport of the surfactant concentration c is achieved by solving for the transport of the Phase Field ϕ (see Eq. (6)). The signed-distance field χ is used to reinitialize the Phase Field ϕ (see Eq. (7)).

where ζ is a velocity scale parameter. For the Phase Field ϕ to be bounded between 0 and 1, $\zeta \geq |u|_{max}$ [71]. In the present study we have used, $\zeta = 1.1|u|_{max}$, ψ is an auxiliary signed-distance-like variable $\psi = \epsilon \log[(\phi+\varepsilon)/(1-\phi+\varepsilon)]$ where $\varepsilon = 10^{-6}$. The use of the Phase Field simplifies the surfactant transport, which involves the calculation of the surface gradient $\nabla_s\Gamma$ (see Eq. 4) [69]. The non-dimensional thickness of the surfactant layer is constant for a given resolution. It is related to the phase-field representation and remains small compared to the flow scale of interest. Typically for a drop or bubble of size d_b, the thickness ratio $N = \epsilon/d_b$ is between 0.03 and 0.0075, and convergence with respect to this thickness ratio is verified when grid convergence tests are performed.

We note that the dense packing of surfactants molecules may alter the interface viscosity, the interface becoming "rigid" at high surfactant concentrations. Interface rheology is a major area of research in colloid and surface physics [1, 89]. In the present work, we have not modeled the rheological effects due to surfactants, so that all processes related to surfactants are linked to surfactants redistribution and Marangoni stresses.

C. Validation of surfactants transport and Marangoni stresses

Here we report the validation of the numerical framework for the transport of the surfactants at the interface coupled with Marangoni stresses (Eqs. 1 - 4). First, surfactant transport, Eq. (4), is tested for interface expansion, advection, and diffusion. Surfactant transport is restricted to the interface and quantitatively agrees with the analytical solutions. Second, the Marangoni stress calculation is tested against a widely used analytical solution [90]. Also, a test for topological changes is provided. Each validation case is reproducible using the corresponding documented source code on the Basilisk website [91].

1. Expansion test

A circle (2D) of diameter d_b is initialized at the center of the computational square domain of side L. Similarly, for the verification of the 3D configuration, a sphere is initialized at the center of a cubic computational domain. The third term on the left-hand side in Eq. (4), $\Gamma(\nabla_s \cdot \mathbf{n})(\mathbf{u} \cdot \mathbf{n})$ accounts for the transport of surfactants due to the expansion of the interface [84]. For a given velocity field $\mathbf{u}(r, \theta, \phi) = Kr\hat{\mathbf{e}}_r$, $\tilde{\Gamma} = \Gamma/\Gamma_0$, $\tilde{\mathbf{u}} = \mathbf{u}/(Kd_b)$, $\tilde{t} = Kt$, and $\mathrm{Pe}_s = Kd_b^2/D_s$, Eq. (4) reduces to

$$\frac{\partial \tilde{\Gamma}}{\partial \tilde{t}} + \tilde{\Gamma}(\tilde{\nabla}_s \cdot \mathbf{n})(\tilde{\mathbf{u}} \cdot \mathbf{n}) = \frac{1}{\mathrm{Pe}_s}\tilde{\nabla}^2\tilde{\Gamma}. \tag{11}$$

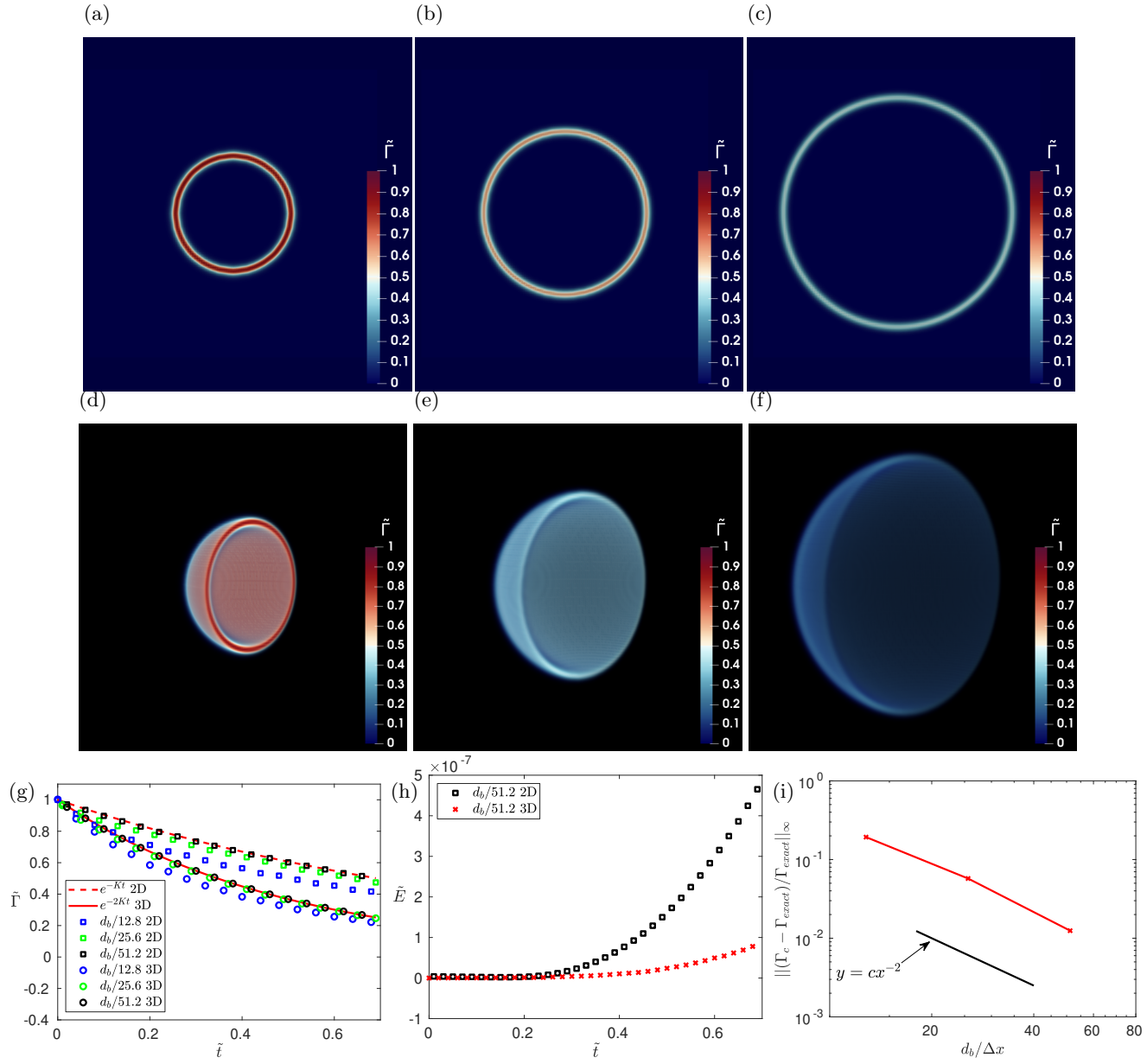

FIG. 2. Normalized surfactant concentration $\tilde{\Gamma}$ on an expanding circle (2D) and sphere (3D) (sliced to show the cross-section) having initial diameter $d_b/L = 0.4$ (a,d) at times $\tilde{t} = 0$, (b,e) $\tilde{t} = 0.35$, and (c,f) $\tilde{t} = 0.7$. (g) Concentration time evolution in 2D and 3D, with a comparison of the numerics (symbols) and theory (solid and dashed). (h) Relative error $\tilde{E} = |m(t) - (m(0))|/m(0)$ of surfactant mass conservation remains below 10^{-6}, where $m(t) = \int_V c(t)\, dv$, (i) Relative error on Γ. These results can be reproduced using the code in [92].

For a uniform surfactant concentration $\tilde{\nabla}_s \tilde{\Gamma} = \mathbf{0}$ and $\mathrm{Pe}_s > 0$, Eq. (11) reduces to

$$\frac{\partial \tilde{\Gamma}}{\partial \tilde{t}} + \tilde{\Gamma}(\tilde{\nabla}_s \cdot \mathbf{n})(\tilde{\mathbf{u}} \cdot \mathbf{n}) = 0, \tag{12}$$

where $(\tilde{\nabla}_s \cdot \mathbf{n})$ and $(\tilde{\mathbf{u}} \cdot \mathbf{n})$ are, respectively, twice the mean curvature and the normal velocity at the interface. Integrating Eq. (12) gives the analytical expression $\tilde{\Gamma}(\tilde{t}) = e^{-\tilde{t}}$ and $\tilde{\Gamma}(\tilde{t}) = e^{-2\tilde{t}}$ for a circle (2D) and a sphere (3D) respectively.

We perform the numerical test for an initial diameter $d_b/L = 0.4$, initial uniform concentration $\tilde{\Gamma}(0) = 1$, $\mathrm{Pe}_s = 16$ and for three uniform resolutions, i.e., $\Delta x = d_b/12.8,\ d_b/25.6,\ d_b/51.2$. Figures 2(a,d), (b,e), (c,f) show the initial ($\tilde{t} = 0$), intermediate ($\tilde{t} = 0.35$), and final ($\tilde{t} = 0.7$) surfactant concentrations on the expanding circle and sphere for the highest resolution. Fig. 2(g) shows the time evolution of surfactant concentration for three different resolutions.

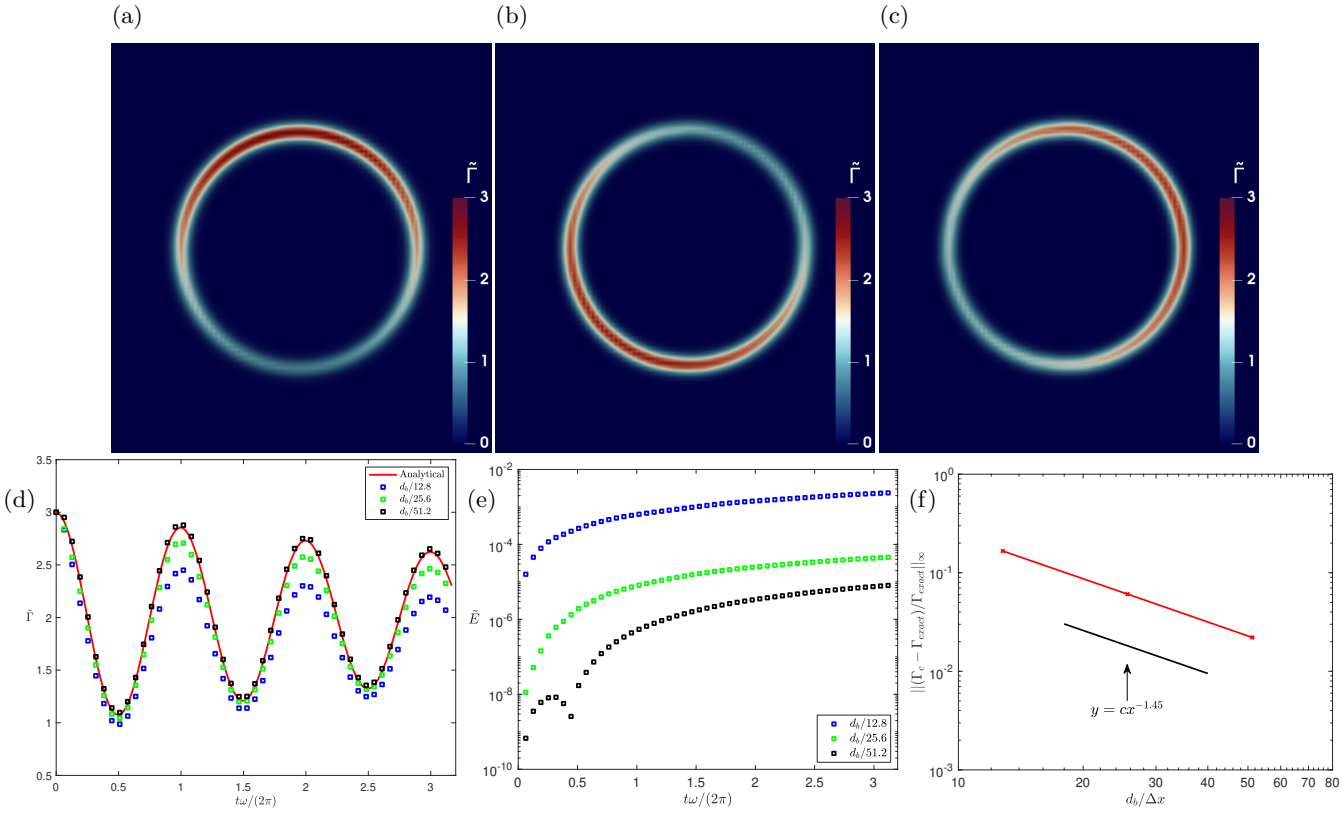

FIG. 3. Surfactant advection test for a rotating circle. Normalized surfactant concentration $\tilde{\Gamma}$ having initial diameter $d_b/L = 0.4$ at (a) $t\omega/(2\pi) = 0$ and (b) $t\omega/(2\pi) = 1.6$ (c) $t\omega/(2\pi) = 3.2$. (d) Concentration time evolution at the zenith of the circle ($\theta = \pi/2$) compared to the analytical solution. (e) The relative error on the total mass of surfactants $\tilde{E} = |m(t) - (m(0))|/m(0)$, where $m(t) = \int_V c(t)\, dv$, remains below $2 \cdot 10^{-3}$ for 12 grid points per diameter and decreases to $2 \cdot 10^{-6}$ when the grid resolution is increased and about 50 grid points per diameter are considered. (f) Relative error on Γ. These results can be reproduced using the code in [93].

With more than twenty grid points per diameter good agreement with the analytical solution (red curve) is obtained. Fig. 2(h) shows the evolution with time of the relative error on surfactant mass: $\tilde{E} = |m(t) - m(0)|/m(0) < 10^{-6}$. The total mass is computed by integrating the concentration c over the computational domain volume V, $m(t) = \int_V c(t)\, dv$. Second-order accuracy can be seen in Fig. 2(i) for the error computed relative to the analytical solution with respect to the number of grid cells per unit diameter $d_b/\Delta x$.

2. *Advection-Diffusion test*

The positivity criterion, $\Delta x \leq 2D_s/(|u|_{max} + D_s/\epsilon)$, or $\mathrm{Pe}_c = |u|_{max}\Delta x/D_s \leq 1$, puts a limit on testing the advection term in Eq. (4) [69]. Therefore, both advection and diffusion are validated in the subsequent single test. We consider a circle of size $d_b/L = 0.4$, initial surfactant concentration as $\tilde{\Gamma}(\theta, 0) = 2 + \sin\theta$ with the flow field representing solid body rotation $\mathbf{u}(r, \theta) = d_b\omega/2\ \mathbf{e}_\theta$. The analytical solution is

$$\tilde{\Gamma}(\theta, \tilde{t}) = 2 + \sin(\tilde{t} + \theta)e^{-4\tilde{t}/\mathrm{Pe}_s} \tag{13}$$

where $\tilde{t} = \omega t$ and $\mathrm{Pe}_s = d_b^2\omega/D_s$. The test is performed for a Péclet number, $\mathrm{Pe}_s = 160$, and three uniform resolutions, i.e., $\Delta x = d_b/12.8,\ d_b/25.6,\ d_b/51.2$. Figure 3(a), (b), and (c) show the initial, intermediate, and final ($t\omega/2\pi = 0.4$, 1.6 and 3.2) surfactant concentrations on the rotating circle for the highest resolution. Figure 3(d) shows the time evolution of surfactant concentration for three different resolutions. Simulations with more than twenty grid points per circle diameter demonstrate good agreement with the analytical solution (red curve). Figure 3(e) shows the time evolution of the relative error on surfactant mass, which remains negligible, as $\tilde{E} = |m(t) - m(0)|/m(0) < 10^{-2}$ for the lowest resolution and $< 10^{-5}$ for the highest resolution. Between first- and second-order convergence can be seen in Fig. 3(f) for the maximum error on surfactant concentration computed relative to the analytical solution with respect to the number of grid cells per unit diameter $d_b/\Delta x$.

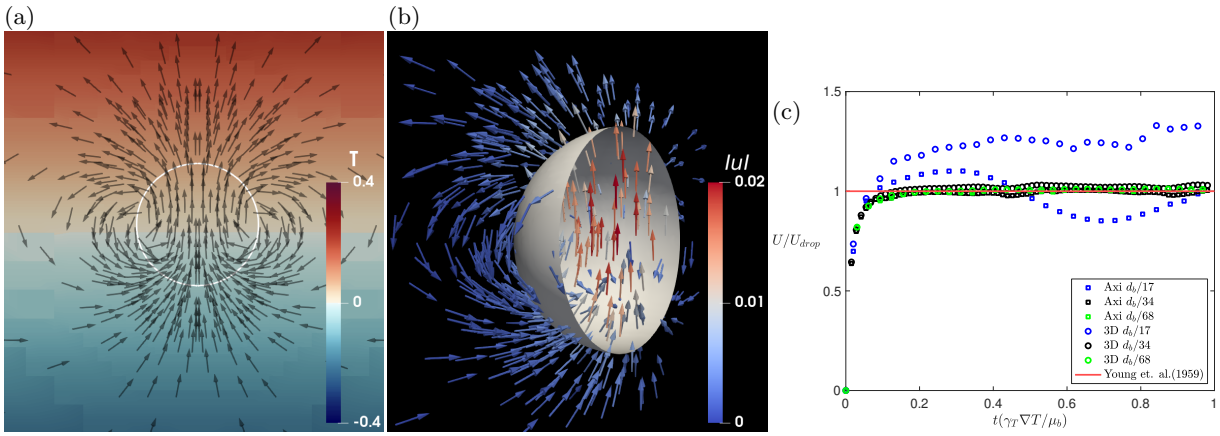

FIG. 4. Migration of a droplet in a thermal gradient (no buoyancy) for $Re = 0.132$, $Ca = 0.066$, $\Delta x = d_b/68$. (a) Axisymmetric droplet interface shown by the white curve, velocity vectors show the direction of migration towards the temperature gradient shown in color. (b) 3D droplet (sliced in half) showing the velocity vectors, with magnitude color-coded. (c) Migration velocity as a function of time. The squares show the velocities of axisymmetric and 3D droplets, respectively, converging towards the theoretical prediction [90] when resolution is increased. These results can be reproduced using the code in [94].

3. *Droplet migration in a thermal gradient*

We test the Marangoni force calculation by considering a droplet (density and viscosity ratio being unity) migrating due to a thermal gradient. The test has been used extensively in earlier studies to validate the Marangoni force calculation [34–36, 95], but does not consider surfactant transport at the interface. The temperature gradient causes a surface tension variation at the interface of the drop and induces thermo-capillary motion. The surface tension is considered a function of temperature, T,

$$\gamma = \gamma_0 + \gamma_T (T - T_0), \tag{14}$$

where T_0 is a reference temperature.

The solution for the migration velocity of a spherical droplet in a constant thermal gradient for small $Re \equiv \rho_l U d_b/\mu_l$ and $Ca = \mu_l U/\gamma_0$ is [90]

$$U_{drop} = -\frac{\gamma_T d_b \nabla T}{\mu_l (6 + 9\mu_b/\mu_l)}. \tag{15}$$

The numerical test is performed for a droplet of diameter d_b, domain $L = 7.5 d_b$, $Re = 0.132$, $Ca = 0.066$, and unity viscosity and density ratios. Fig. 4(a) and (b) show, respectively, axisymmetric, two-dimensional and three-dimensional droplets migrating in a thermal gradient. The droplet migrates towards warmer regions due to the non-equilibrium force created by variable surface tension. The vectors show the direction of the local velocity. Fig. 4(c) shows the time evolution of the velocity of the center of mass of the droplet. At the lowest grid resolution of 16 cells per diameter, the migration velocity oscillates around the value predicted by Eq. (15). When the resolution is increased above 34 cells per droplet diameter, the migration velocity becomes independent of the grid resolution with converged results between 34 and 68 grid points per diameter and in good agreement with the analytical prediction, for both the axisymmetric and 3D configurations.

4. *Surfactant transport with topological changes due to the Plateau–Rayleigh instability*

Breakup and coalescence, which result in topological changes of the interface, are key phenomena in interfacial flows. We test the present framework for mass conservation during topological changes by considering the classical Plateau–Rayleigh instability occurring in cylindrical jets and threads. We initialize an axisymmetric cylindrical thread having diameter d_b, density ρ_b, and viscosity μ_b perturbed axially with wavenumber k in a fluid having density ρ_l and viscosity μ_l. The fluid properties are set to $\rho_b/\rho_l = 1$, $\mu_b/\mu_l = 100$, $\mathrm{Oh} = \mu_b/\sqrt{\rho_b \gamma d_b} = 0.01$ and $\mathrm{Pe}_s = \sqrt{\gamma/(k\rho_b)}/D_s = 10$, where γ and D_s are, respectively, the surface tension between the fluids and surfactant diffusivity. Such a configuration is prone to the Plateau–Rayleigh instability.

Figure 5 shows the surfactant concentration and the interface at different times during the Plateau–Rayleigh process. Figure 5(a) shows the thread initially perturbed as $2r(z)/d_b = 1 - 2a_p/d_b \cos(kz)$ with $kd_b = 0.2\pi$, and $a_p/d_b = 0.2$.

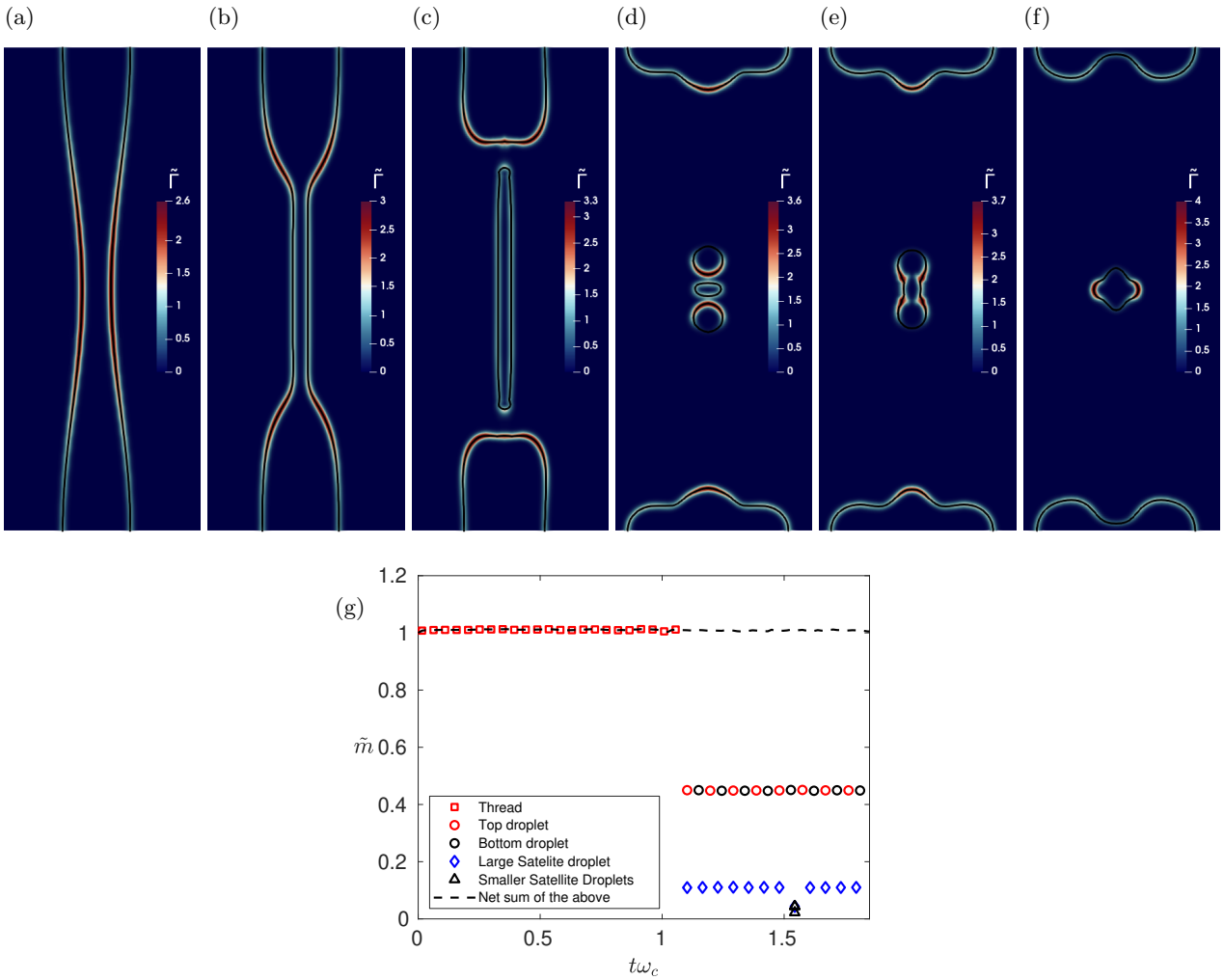

FIG. 5. Time stills showing surfactant concentration (blue-red) and interface (Shown by the thin black line inside the concentration field) of an axisymmetric thread undergoing a Plateau–Rayleigh instability. (a) $t\omega_c = 0$: the initial condition of the perturbed thread; (b) $t\omega_c = 0.94$: thinning of the thread before breakup; (c) $t\omega_c = 1.1$: surfactants remain at the interface after the breakup; (d) $t\omega = 1.57$: subsequent breakup and satellite droplet formation; (e) $t\omega = 1.6$: coalescence of satellite droplets; (f) $t\omega_c = 1.73$: oscillations before equilibrium state. (g) surfactant mass budget. During break-up and coalescence, the surfactants remain on the interface and their total mass is conserved. These results can be reproduced using the code in [96].

A non-uniform surfactant distribution is initialized as $\tilde{\Gamma} = \Gamma/\Gamma_0 = 1 + \Gamma_p/\Gamma_0 \cos(kz)$ with $\Gamma_p/\Gamma_0 = 0.5$. The surface tension is kept constant throughout as we test only the surfactant transport in a configuration involving topological changes. The cylindrical fluid thread predictably undergoes the Plateau–Rayleigh instability as $kd_b/2 < 1$. Figures 5(a-f) show the interface and surfactant concentration at different times non-dimensionalized by $\omega_c = \sqrt{\gamma k^3/\rho_b}$. In Figure 5(b), $t\omega_c = 0.94$, a thinning of the thread occurs before the breakup where the surfactants are moved away from the central part of the thread. The breakup is a topological change where the thread interface is broken into three parts and shown in Figure 5(c) at $t\omega_c = 1.1$. The surfactant concentration remains restricted to the interface without any singular values, and mass is conserved. The mass of the surfactants is calculated on the interfaces of the initial thread and the individual droplets $\tilde{m} = \int c(t)\, dv / \int c(0)\, dv$ are shown in Figure 5(g), where we observe that the mass from the thread (red squares) is distributed during the breakup among the top (red circles) and bottom (black circles) drops as well as in a satellite drop (blue diamonds). In Figure 5(d), $t\omega_c = 1.57$, the subsequent retraction of the central droplet further breaks into three droplets (black triangles in Figure 5(g)) before coalescing in Figure 5(e) at $t\omega_c = 1.6$, with the redistribution of surfactants being well captured in both cases. Figure 5(f), $t\omega_c = 1.73$, shows the oscillations of droplets before reaching equilibrium. The net sum of distributed mass among all the droplets is shown as a black dashed line in Figure 5(g), demonstrating satisfactory mass conservation.

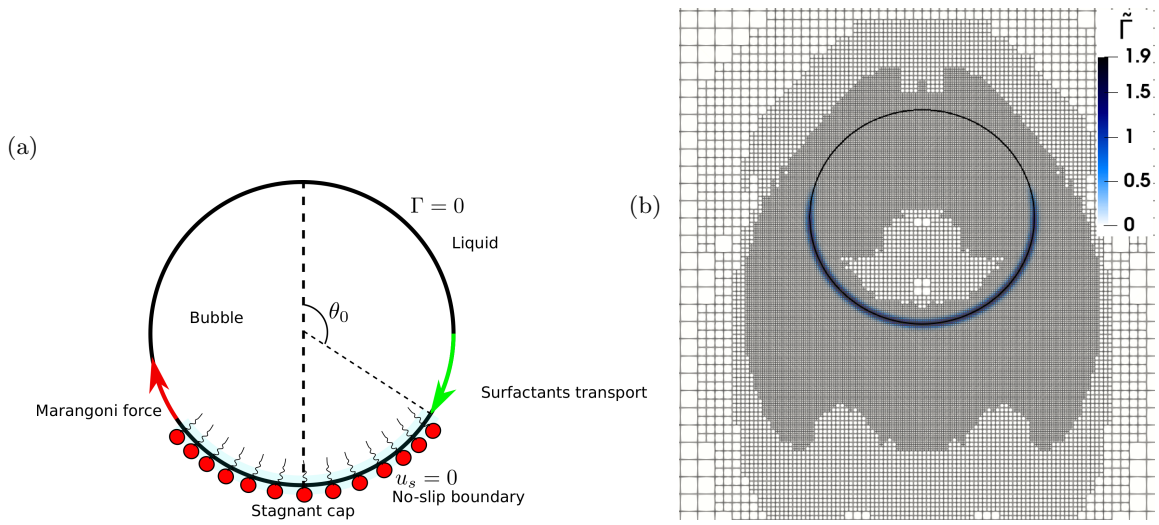

FIG. 6. (a) Schematic of a rising bubble at the terminal state in the presence of surfactants. The stagnant cap angle θ_0 is measured from the apex of the bubble. Figure adapted from [97]. (b) Still image from the present study, illustrating the bubble interface (solid black line), the surfactant concentration (blue colors, with dark blue indicating higher concentration), and the formation of the stagnant cap at the rear of the bubble. The adaptive mesh refinement (AMR) around the bubble is shown for L11, $\Delta x = L/2^{11}$, with the number of cells of $\approx 1.4 \times 10^4$ yielding a significantly smaller number of grid points than a simulation with a uniform grid for which the number of cells would be $(2^{11})^2 \approx 4.2 \times 10^6$.

5. *Advantages and limitations of the numerical framework for surfactant transport*

Our numerical framework is thus validated for the transport of surfactants, the Marangoni force calculation, and topological changes. The method accuracy is between first and second order and a simple implementation avoids the calculation of surface derivatives on a moving fluid-fluid interface for surfactant transport. Therefore, it is adaptable to various other numerical frameworks and efficient in investigating two- and three-dimensional two-phase flow problems. The anti-diffusion term is added to the surfactant transport equation to maintain a sharp distribution of surfactant concentration near the interface. The numerical scheme hence requires an increase in resolution with the increase in Péclet number, which makes it prohibitive for high Péclet regimes. In the next section, we investigate the rise of a bubble laden with insoluble surfactants as an illustration of the framework capabilities.

III. EFFECT OF SURFACTANTS ON RISING BUBBLES

A. Problem statement

Experimental data summarized by Clift *et al.* [98] from Grace [99] provide an empirical prediction of a bubble's terminal velocity and terminal shape given a set of two independent parameters, $\mathrm{Ga} = \rho_l d_b \sqrt{g d_b}/\mu_l$ and $\mathrm{Bo} = \rho_l g d_b^2/\gamma_0$, where d_b is the diameter of the undeformed bubble, which compares viscosity, gravity, and surface tension effects, respectively. The bubble's terminal velocity can then be expressed as a non-dimensional number, usually either expressed as a Reynolds number or a drag coefficient, which is a function of the other two non-dimensional numbers Bo and Ga.

For small Bo and Ga, slow-moving spherical bubbles (creeping flow), **?**] and Rybczynski [100] independently found the solution for the terminal velocity. However, the Hadamard-Rybczynski theory of internal circulation and terminal velocity is not commonly observed. The absence of internal circulation can be related to surfactants, which tend to accumulate at the interface resulting in a surface-tension gradient that causes tangential stresses that oppose surface motion [21, 22]. Direct Numerical Simulations (DNS) of a weakly soluble surfactant-laden axisymmetric bubble were carried out by Cuenot *et al.* [28] confirming the stagnant cap model and drag reduction, and the dependence on stagnant cap angle proposed by Sadhal and Johnson [25]. Later, the effect of adsorption/desorption of soluble surfactants was investigated by Lakshmanan and Ehrhard [48] for axisymmetric bubbles.

Apart from the terminal velocity and shape, a phenomenon that has been an active area of research is the transition from a straight to non-straight (either helicoidal or zigzag) path of a rising bubble observed for a certain range of

Geometry	Ga	Bo	Ma	Resolution ($d_b/\Delta x$)
2D Axisymmetric	5	0.5	$0-20$	$25, 50, 100$
	10	0.5	$0-20$	$25, 50, 100$
	25	0.5	$0-20$	$25, 50, 100$
	50	0.5	$0-20$	$25, 50, 100$
	100	0.5	$0-20$	$25, 50, 100$
3D	100.25	10	$0, 1$	$25, 50$

TABLE II. List of simulations for various Ga, Bo, and Ma.

parameters (e.g., Krishna and Baten [101], Magnaudet and Eames [102], Ohl *et al.* [103], Prosperetti [104]). Mougin and Magnaudet [105] and Tchoufag *et al.* [106] consider freely-moving oblate spheroidal bubbles and show that frozen-shaped bubbles with sufficient oblateness are unstable in certain parameter ranges (then leading to helicoidal or zigzag paths). The DNS from Mougin and Magnaudet [105] are mostly performed far from the threshold for path instability. These studies show that the path instability may arise in ranges of parameters where the wake alone is still stable (for parameters far from threshold values, the wake is indeed also unstable). Further direct numerical simulations and analysis by Cano-Lozano *et al.* [107], Bonnefis [108] and Bonnefis *et al.* [109] have characterized the region of parameters with stable and unstable paths in terms of the Bond and Galileo numbers, discussing thresholds for instability in the path, as well as frequency of oscillations for both deformable and frozen interfaces. Subsequently, Herrada and Eggers [110] performed global linear stability analyses of freely deformable bubbles in regimes relevant to air bubbles in water.

In the present study, we explore the effect of surfactants on a rising bubble in both axisymmetric and three-dimensional configurations. Figure 6(a) sketches the qualitative features of a rising bubble laden with insoluble surfactants. The surface-restricted transport concentrates the surfactants at the rear of the bubble and creates a gradient of surface tension resulting in Marangoni forces in the direction of this gradient $\nabla_s \gamma$, slowing down the bubble.

The effect of surfactants transported along the interface therefore introduces a non-dimensional parameter, the Marangoni number, comparing surface tension gradient effects and surfactant advection. Here we consider the characteristic velocity $\sqrt{gd_b}$ and define $\mathrm{Ma} = \beta\gamma_0/\sqrt{gd_b}\mu_l$, where β is the Gibbs elasticity. The Gibbs elasticity is related to the surfactant isotherm provided in Eq. (5). Next, using our numerical framework we explore the role of Ma on the bubble rise velocity and demonstrate that several classical results can be retrieved and quantified.

B. Approach: Direct Numerical Simulations

We perform 3D and axisymmetric DNS of a single buoyant bubble (subscript b) of undeformed diameter d_b in a denser quiescent liquid (subscript l). The domain uses periodic boundary conditions and is of size $L = 20d_b$. The computational domain is resolved using adaptive mesh refinement (as illustrated in Figure 6(b)) by having 25-100 grid cells per diameter of the bubble, with the high-resolution grid being focused on the bubble interface and the boundary layer around it. The chosen adaptivity criterion allows us to properly resolve the influence of the bubble's wake on its dynamics while making sure that given the periodic boundary conditions, the bubble is not influenced by the previous wake.

Three different resolutions are considered, with the smallest grid size Δx being L9 with $\Delta x \equiv L/2^9 \equiv d_b/25$, L10 with $\Delta x \equiv L/2^{10} \equiv d_b/50$, and L11 with $\Delta x \equiv L/2^{11} \equiv d_b/100$. Figure 6(b) shows a snapshot from one simulation, where the bubble interface is shown by the solid black curve, and illustrates the adaptive grid and the formation of the stagnant cap, where the surfactants (in color, with red regions corresponding to high surfactant concentration and blue regions to low concentration) are concentrated at the bottom of the bubble. The adaptive mesh refinement (AMR) around the bubble shown for L11 $\Delta x = L/2^{11}$ keeps computational cost low, as our simulations at L11 involve $\approx 1.4 \times 10^4$ grid points in 2D (axisymmetric) and $\approx 4 \times 10^6$ in 3D. Comparing such resolution on the bubble to a uniformly-refined domain, the number of cells would be $(2^{11})^2 \approx 4.2 \times 10^6$ and $(2^{11})^3 \approx 8.6 \times 10^9$ for 2D (axisymmetric) and 3D, respectively, demonstrating the interest of AMR for such flows. Grid convergence is achieved as demonstrated in Appendix A.

We consider the case where surfactant transport is convection-dominated, so that the Péclet number is large; here $\mathrm{Pe}_s \equiv d_b\sqrt{gd_b}/D_s = 100$ (using $\sqrt{gd_b}$ as the characteristic advection velocity). We consider large density and viscosity ratios $\rho_l/\rho_b = 1000$ and $\mu_l/\mu_b = 100$. We limit the axisymmetric simulations in Table II to the region where the rising bubble (without surfactants) remains spheroidal and the path is rectilinear, as observed by Cano-Lozano *et al.* [107]. Three-dimensional simulations consider cases showing helicoidal and zigzag trajectories as discussed in the numerical

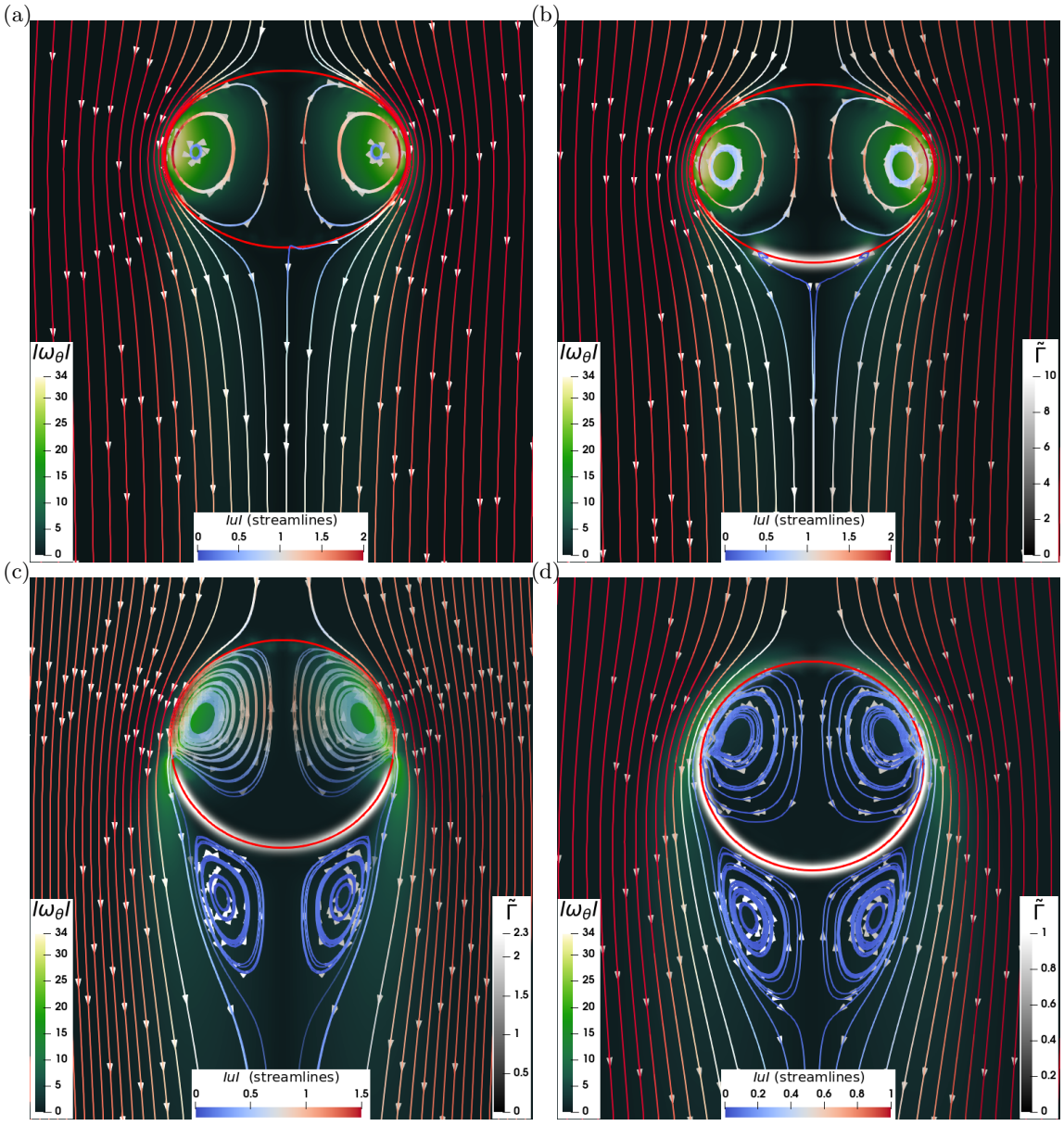

FIG. 7. Bubble shape, dynamics, and surfactant concentration at steady (terminal velocity) state for Ga = 100 and Bo = 0.5, for a clean bubble (a) Ma = 0, and increasing contamination so that (b) Ma = 0.2, (c) Ma = 2, and (d) Ma = 20. The thick red curve shows the bubble's (sharp) interface (obtained through geometric VoF reconstruction). Flow around the bubble is visualized through the streamlines (blue-red) in the reference frame of the bubble, shown with lines and arrows; vorticity is colored black-green-white. Surfactant concentration is colored black-white (and localized at the interface). The addition of surfactants shows the immobilization of the interface with increasing Ma number. The streamlines show the structure of the bubble's wake. Examining the magnitude of the velocity inside the bubble confirms the reduction of the internal circulation.

work from Cano-Lozano *et al.* [107] as well as in the experiments from Tagawa *et al.* [111].

As discussed above, we consider a linear isotherm, Eq. (5). Experimental observations have shown that the maximum reduction in surface tension achieved is surfactant-specific [112], with the maximum packing concentration of surfactants limiting a further decrease in the surface tension to $\gamma_\infty/\gamma_0 \approx 0.2-0.6$ [16, 113]. In the present study, the transport of surfactants is restricted to the interface and no desorption and adsorption are considered. A minimum threshold value of surface tension has been used in independent numerical studies by [32, 114] to avoid reaching negative values. In the present study, we found that a sharp threshold value produces a surface tension gradient that is always grid dependent. Therefore, we consider a smooth isotherm $\gamma(\mathbf{x},t) = \gamma_0(1 - \tanh[\beta\Gamma(\mathbf{x},t)/\Gamma_0])$ that behaves as Eq. (5) for $\beta\Gamma(\mathbf{x},t)/\Gamma_0 \to 0$ and approaches zero as $\beta\Gamma(\mathbf{x},t)/\Gamma_0 \to \infty$. We have verified that this isotherm behaves as Eq. (5), remains grid independent, and does not affect the bubble rise terminal velocity and trajectory.

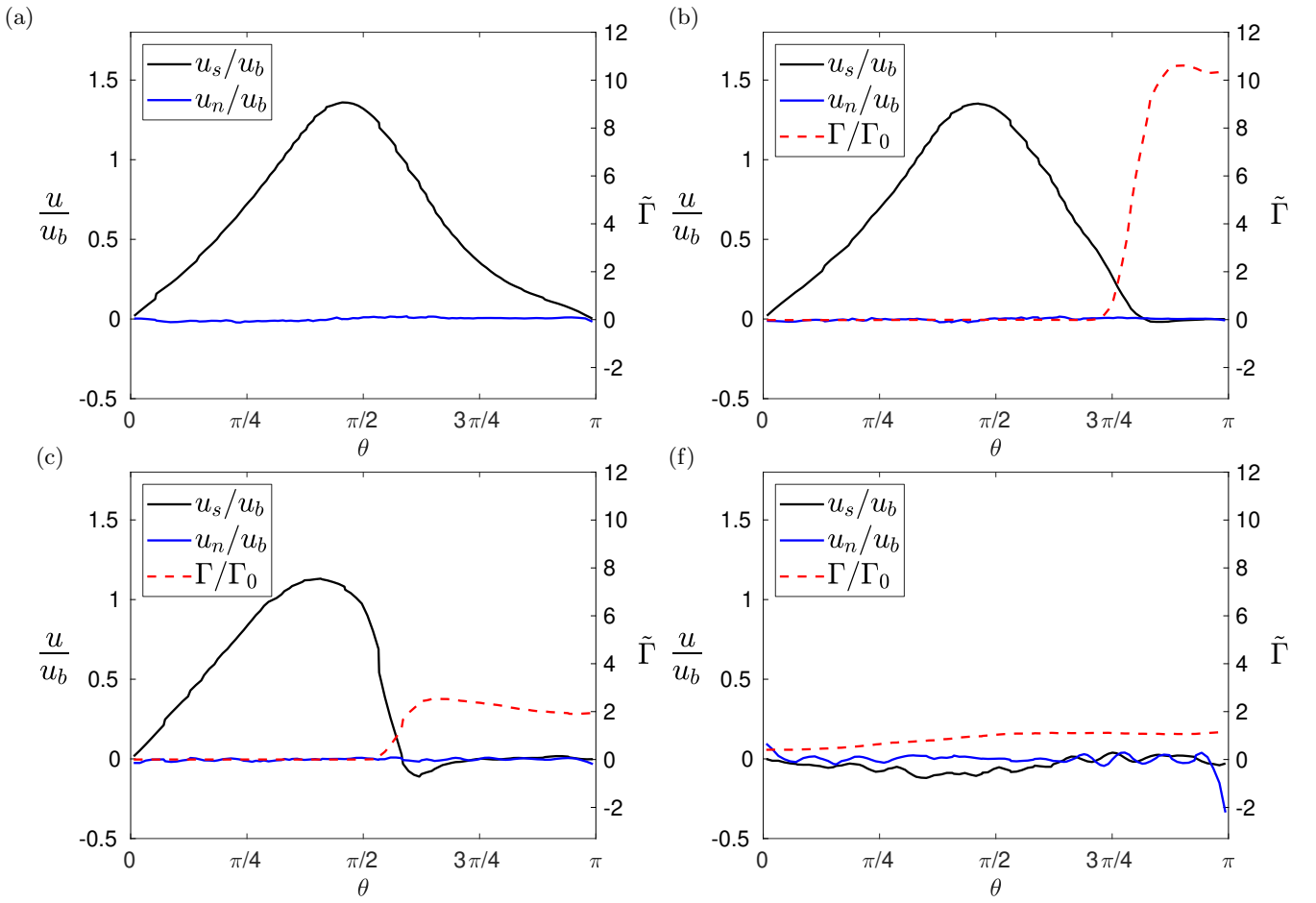

FIG. 8. Interfacial velocity in the reference frame of the bubble for Ga = 100 and Bo = 0.5 at steady (terminal) state $t\sqrt{g/d_b} = 5$ as a function of the polar angle θ measured from the apex of the bubble. (a) Ma = 0 (b) Ma = 0.2 (c) Ma = 2 (d) Ma = 20. The tangential component u_s/u_b (black) and normal u_n/u_b (blue) of the bubble are shown. The normal component is zero as there is no flow across the bubble. The normalized surfactant concentration $\tilde{\Gamma} = \Gamma/\Gamma_0$ is shown in red, with the corresponding axis on the right. The tangential velocity vanishes at the stagnant cap angle θ_0. The stagnant cap angle corresponds to the vanishing tangential velocity and is $\theta_0 = \pi$ for a clean bubble. The stagnant cap angle decreases as the Marangoni number is increased, and also corresponds to the maximum surfactant concentration. The presence of a small concentration of Γ below the stagnant cap angle $\theta < \theta_0$ is caused by the non-zero surface diffusivity of surfactants $D_s > 0$.

C. Effect of the Marangoni number on the terminal axisymmetric rise velocity

We now present a systematic study of axisymmetric bubbles rising in clean and contaminated conditions, i.e., surfactants are present at the interface, for a wide range of non-dimensional parameters, as summarized in Table 2, varying Ga from 5 to 100 and keeping Bo= 0.5 while Ma varies from 0 (clean) to 20. Figure 7 shows the terminal state from the axisymmetric simulations of a rising bubble at various Ma for Ga = 100 and Bo = 0.5 and illustrates the effect of surfactants and Marangoni stresses on rising bubbles. The streamlines and vorticity field are plotted from the reference frame of the rising bubble and illustrate the flow structure, while the surfactant concentration is also shown. The effect of increasing the Ma number is remarkable in several aspects.

The clean bubble corresponding to Ma = 0 is shown in Figure 7(a). We observe that the high vorticity region is inside the bubble due to the internal circulation of lower-viscosity gas driven by the liquid outside and streamlines show that the flow is qualitatively similar to a potential flow outside the bubble.

The other snapshots (Figure 7b,c,d) show, for increasing Marangoni numbers, the flow features when the terminal velocity is reached once surfactants have been introduced. Figure 7(b) shows Ma = 0.2, with surfactants concentrated at the rear of the bubble and a stagnant cap formed at the rear of the bubble due to the surface immobilization, itself a consequence of the Marangoni force acting in the direction opposite to the surfactants flow. The effect of surfactants is therefore similar to a no-slip condition, which arises at the stagnant cap and a flow separation can be seen from the ends of the stagnant cap. The streamlines show that a standing eddy starts to form behind the bubble. As the

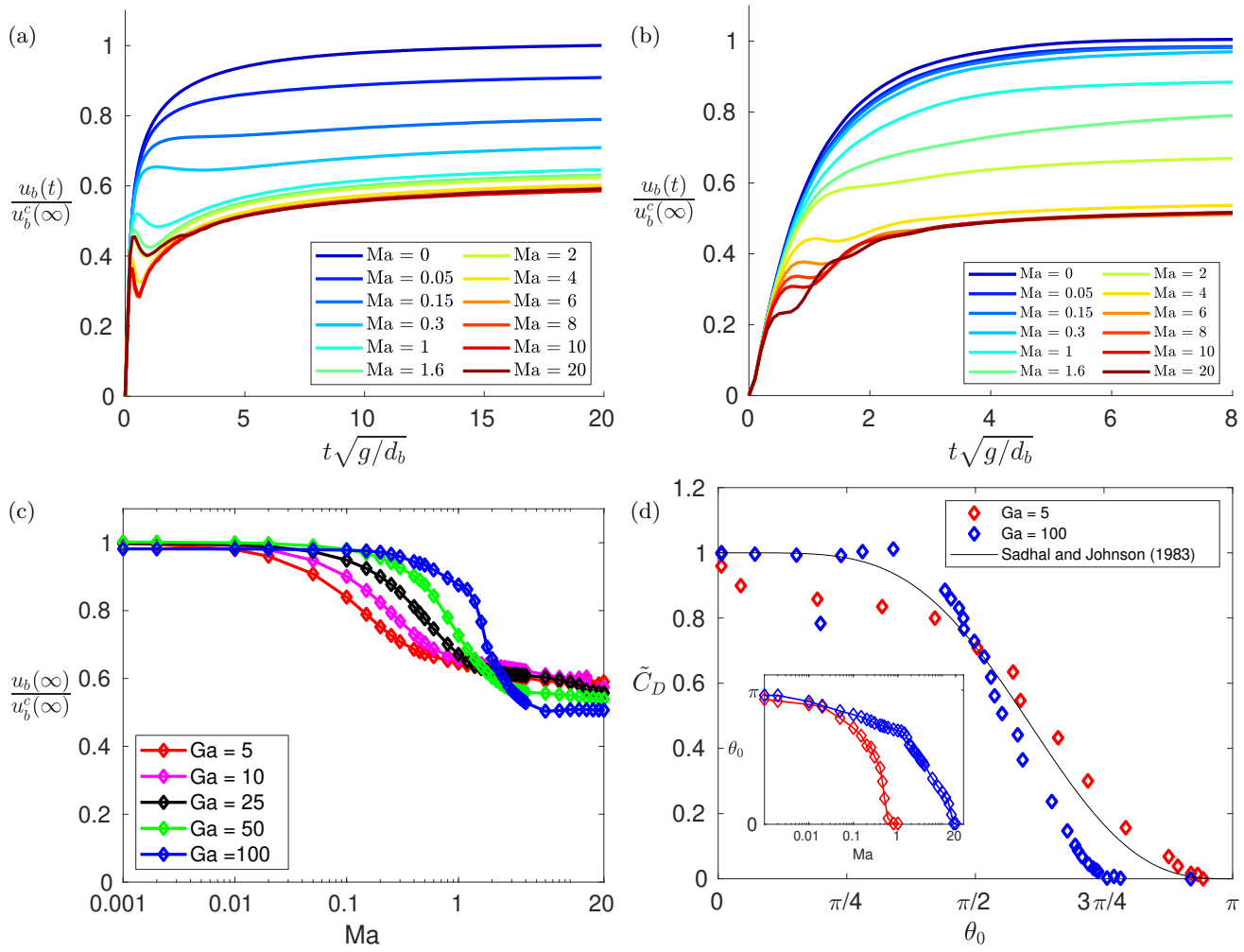

FIG. 9. (a,b) Evolution of the bubble rise velocity as a function of time for Bo = 0.5 and (a) Ga = 5, (b) Ga = 100 for a grid resolution $\Delta x = d_b/50$. The Ma number increases from 0 (clean bubble) to 2 from blue to red. The terminal velocity of the bubble decreases with an increase in Ma, while the reduction of the rise speed saturates at high Ma. (c) Effect of the Marangoni number on the terminal velocity, normalized by the terminal velocity in the clean case $u_b(\infty)/u_b^c(\infty)$. Marangoni effects start to be important for smaller values of Ma for smaller Ga. All curves saturate for $Ma > 10$. (d) Normalized drag coefficient $(C_D - C_{rigid})/(C_{rigid} - C_{clean})$ as a function of the stagnant cap angle, which decreases with Ma. The clean bubble has $\theta_0 = \pi$ and large surfactant effects (high Ma) lead to $\theta_0 = 0$, which corresponds to the rigid sphere case. Numerical data are compared to the theoretical curve from Sadhal and Johnson [25] (black line). Inset shows the variation of the stagnant cap angle with an increase of the Marangoni number. The reduction of rise velocity plateaus as $\theta_0 \to 0$.

Marangoni number increases from 0.2 to 2 (Figure 7(c,d)), the stagnant cap and standing eddy expand, and there is a change in the bubble shape, which gets more spherical. In the figure panels, the streamlines are colored with the magnitude of velocity, which confirms the reduction in internal circulation as the surface is entirely immobilized due to the Marangoni force.

Figure 8 shows the interfacial velocity in the reference frame of the bubble, for the same cases as in Figure 7, as a function of the polar angle θ measured from the apex of the bubble (Figure 6(a)). The velocity is decomposed into a normal component and a tangential component (the normal component being 0 in the frame of reference of the bubble). In the case without surfactants (Figure 8a, Ma=0), the interfacial velocity's tangential component increases and reaches a maximum around a polar angle $\theta = \pi/2$ and then decreases to zero at the bottom point of the bubble, which is the stagnation point for a clean bubble. These features are qualitatively consistent with the potential flow solution. The stagnant cap angle for this case is thus $\theta_0 = \pi$.

As Ma increases, e.g., Ma= 0.2 in Figure 8(b), the tangential component of the bubble velocity goes to zero before the bottom point of the bubble, so that the stagnant cap angle is $3\pi/4 < \theta_0 < \pi$, and reaches $\pi/2 < \theta_0 < 3\pi/4$ for Ma = 2 (Figure 7(c) and Figure 8(c)) and $\theta_0 \approx 0$ for Ma = 20 (Figure 7(d) and Figure 8(d)) where the stagnant

cap covers a larger surface area of the bubble and, correspondingly, the surface is immobilized. These effects produce stronger standing eddies in the wake of the bubble and increase the drag and hence further decrease the rise velocity. Also, the shape of the bubble is changed from oblate to spherical as Ma is increased. The stagnant cap angle θ_0 corresponds to the location where the tangential velocity u_s reaches zero. For $\theta > \theta_0$ the surfactants accumulate, as indicated by the red dashed line in Figure 8(b-d), which shows the surfactant concentration as a function of θ. The presence of surfactants for $\theta < \theta_0$ is due to the competition between the diffusive transport and advective transport, i.e., $D_s \left|\nabla\Gamma\right| > u_s\Gamma$ or $\mathrm{Pe}_s = u_s d_b/D_s < d_b \left|\nabla\Gamma\right|/\Gamma$. As $\mathrm{Pe}_s \to \infty$, the surfactant concentration at the stagnant cap angle $\Gamma(\theta_0)$ tends to zero.

The clean bubble case Ma = 0 reaches a terminal velocity $u_b^c(\infty)$, which is reduced when surfactants are introduced and as the strength of the Marangoni stresses is increased (increasing Ma). Figure 9 shows the time evolution of the rise velocity normalized by the terminal velocity of the clean bubble, $u_b(t)/(u_b^c(\infty))$, for (a) Ga = 5 and (b) Ga = 100 with Bo = 0.5 and increasing Marangoni numbers. Similar trends are observed for all Ga and Bo tested, and results are grid converged as demonstrated in Appendix A. Increasing Ma leads to a decrease in the rise velocity at all times, and the transient regime is longer when the Marangoni number Ma is increased. The transient regime is affected by the transport of the surfactants on the interface of the bubble, and in contaminated cases, the terminal velocity is only achieved once the surfactant concentration along the bubble has reached a steady state (e.g., see Figure 7). The terminal rise velocity for both values of Ga decreases as Ma is increased, as seen in Figures 9a and 9b. A larger Ma is required for Ga = 100 to reach a similar reduction in velocity, as a higher Marangoni force is required to counteract the force of buoyancy. At sufficiently high Ma, the reduction saturates, with a similar reduction in velocity for Ma=10 and 20 for all Ga.

The change in the terminal velocity, normalized by the terminal velocity of a clean bubble $u_b(\infty)/u_b^c(\infty)$, with increasing Ma for a range of Ga $= 5 - 100$ (and Bo = 0.5) is reported in Figure 9(c). The sensitivity to the Marangoni number on the terminal velocity decreases as the Galileo number is increased, in the sense that a higher Ma is necessary to start observing a decrease in rise velocity. For example, we observe a reduction of 20% in rise velocity at Ma=0.1 for Ga=5, while Ma=1 is necessary at Ga=50. However, in all cases, a decrease in rise velocity is observed for Ma > 1, and the reduction in rise velocity plateaus for Ma > 5. The rise velocity reduction for Ma $\gg 1$ increases slightly from about 50% to 60% when increasing Ga. The transition from a clean to completely contaminated terminal rise velocity occurs over a very sharp gradient in Ma number at high Ga while a smooth transition is observed at low Ga.

The behavior described in Figure 9c when increasing the Marangoni number is in good agreement with the observations reported in experiments by Bel Fdhila and Duineveld [27], where a plot similar to ours is presented with the concentration of surfactants used for the x-axis instead of Ma number. A quantitative comparison of the effect of surfactants on the rise velocity with experimental data is challenging because we would need to be able to link the bulk concentration reported experimentally to the bubble surface concentration (which is difficult to measure), while also requiring experimental data on the specific isotherm from the experiment (the isotherm being surfactant-specific; see the discussion in Manikantan and Squires [20]). Indeed, the details of the curve shown in figure 9c are expected to be sensitive to the details of the surface isotherm, which vary with the type of surfactants. However, the general behavior of retardation of rise velocity is consistent.

Next, a normalized drag coefficient is defined as $\tilde{C}_D = (C_D - C_{rigid})/(C_{rigid} - C_{clean})$, where C_{rigid} and C_{clean} are the drag coefficients for the bubble having stagnant cap angle $\theta_0 = 0$ and $\theta_0 = \pi/2$ respectively (clean and completely contaminated cases) and the standard drag coefficient is calculated from the terminal rise velocity as $C_D = 4gd_b/(3(u_b(\infty))^2)$. The corresponding results for Ga = 5 and Ga = 100 are shown in Figure 9(d). For high Ma, the stagnant cap angle is close to zero, the bubble has a completely immobilized interface, and the drag coefficient corresponds to that of a rigid sphere. Similarly, for low Ma, the interface is mobile and the drag coefficient corresponds to the one from a clean bubble. The inset in Figure 9(d) shows the variation of the stagnant cap angle θ_0 as the Marangoni number increases from Ga = 5 to 100. This provides an effective way to translate the Marangoni number into the stagnant cap angle (for different Ga numbers) and finally to the drag coefficient $\tilde{C}_D$.

Even though the equivalent Reynolds number is not necessarily low, the dependence of the drag coefficient as a function of the stagnant cap angle follows a trend predicted for creeping flows by Sadhal and Johnson [25]. Other independent numerical studies by Cuenot *et al.* [28] and Kentheswaran *et al.* [97] have found similar trends for drag coefficient as a function of stagnant cap angle θ_0. This suggests that a simple parameterization for the drag coefficient (or reduction in rise speed) could be proposed as a function of the Marangoni number Ma.

D. Three-dimensional motion of bubbles: spiral and zigzag trajectories

Three-dimensional simulations of surfactant-laden bubbles are necessary to explore the transitions from rectilinear (straight path) to complex paths (helicoidal or zigzag motion), with implications for applications involving large bubbles in contaminated water (at the ocean–atmosphere interface or in bubble column reactors for example).

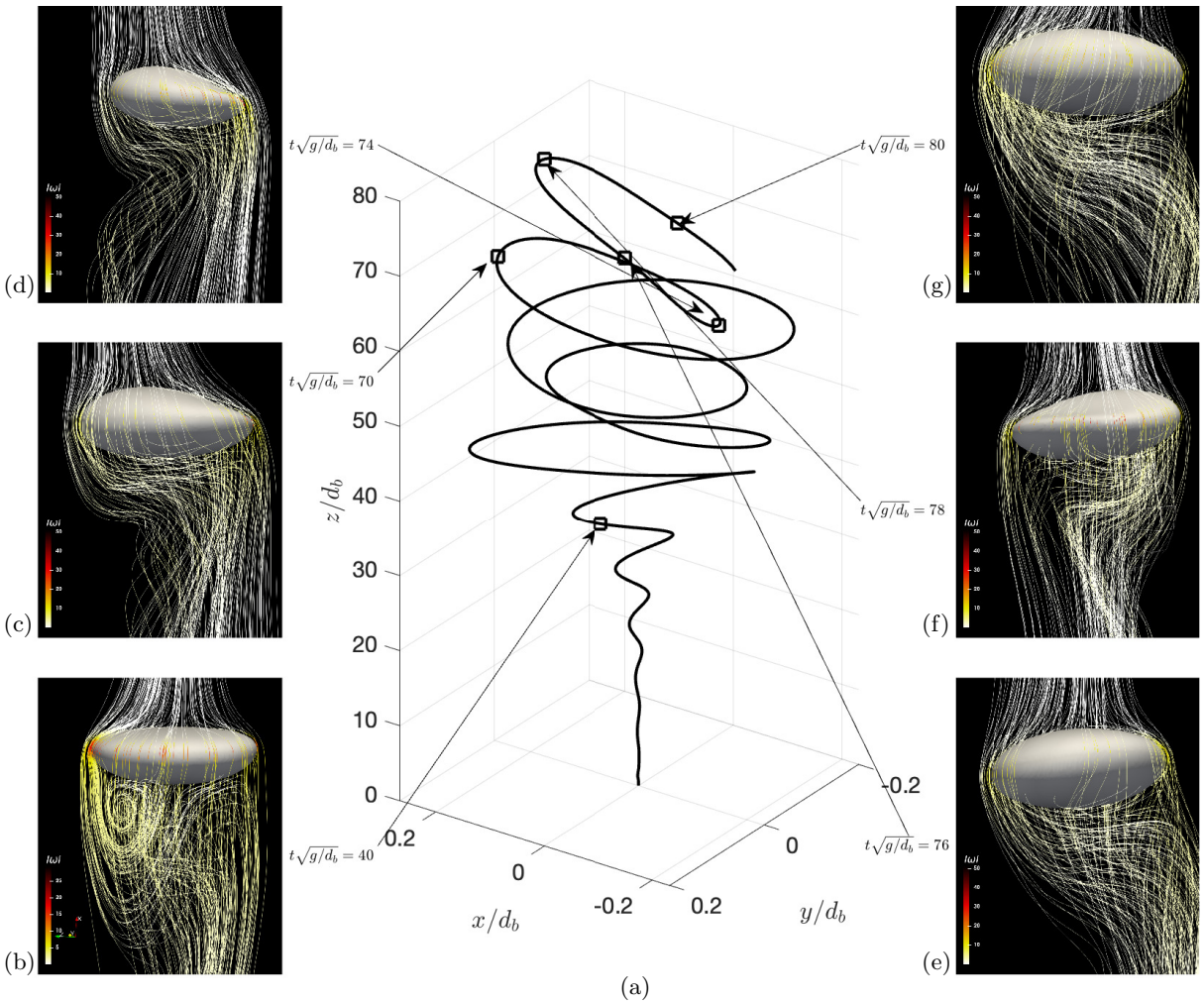

FIG. 10. Bubble trajectory and associated snapshots showing the bubble shape and surrounding flow for Ga = 100.25 and Bo = 10; in the clean configuration Ma = 0. (a) Trajectory evolution, for $t\sqrt{g/d_b} = 0 - 83$. The streamlines calculated from the reference frame of the bubble are shown around the bubble in (b-g) at different time instants. The clean bubble follows a spiraling trajectory.

Investigations using numerical simulations complement experimental studies [111], allowing to change the surfactant isotherm, surfactant concentration, and systematically vary the different controlling parameters. Such systematic studies could help better understand the various transitions between straight, zigzag, and helical paths, as well as the mechanisms behind each dynamical regime. We demonstrate here the capabilities of our numerical framework in performing such three-dimensional simulations of surfactant-laden bubbles rising in a quiescent fluid.

We consider three-dimensional simulations for a set of parameters from Cano-Lozano *et al.* [107] where path instability of a rising bubble is observed in clean conditions: Ga = 100.25, Bo = 10, and the bubble follows a spiral trajectory under clean conditions. We use adaptive mesh refinement with a number of grid points per diameter of 50 (level of refinement 10), so that the main properties of the trajectory (type of path, frequency of oscillation, terminal rise velocity) is expected to be grid converged (see discussion in Cano-Lozano *et al.* [107] and axisymmetric results for the terminal velocity in the appendix). The trajectories, oscillation frequency, and the rise velocity in the clean case are comparable to those reported in Cano-Lozano *et al.* [107].

Figure 10(a) shows the bubble trajectory for the clean case (i.e., Ma = 0). Figure 10(b-g) show the bubble interface and streamlines for one circular cycle $70 \leq t\sqrt{g/d_b} \leq 80$. The bubble starts rising and attains an oblate shape (b) with a recirculating wake at the rear of the bubble. The recirculating wake is observed until the start of the spiraling motion i.e., $0 < t\sqrt{g/d_b} \lessapprox 40$ (b), with a change in the structure of the streamlines once the spiraling motion is in progress (see c d, e, f, g) for times after $t\sqrt{g/d_b} \gtrapprox 60$. Throughout these times, the bubble oscillates as it rises on a helicoidal path. The wake presents mostly open streamlines during the helicoidal oscillations.

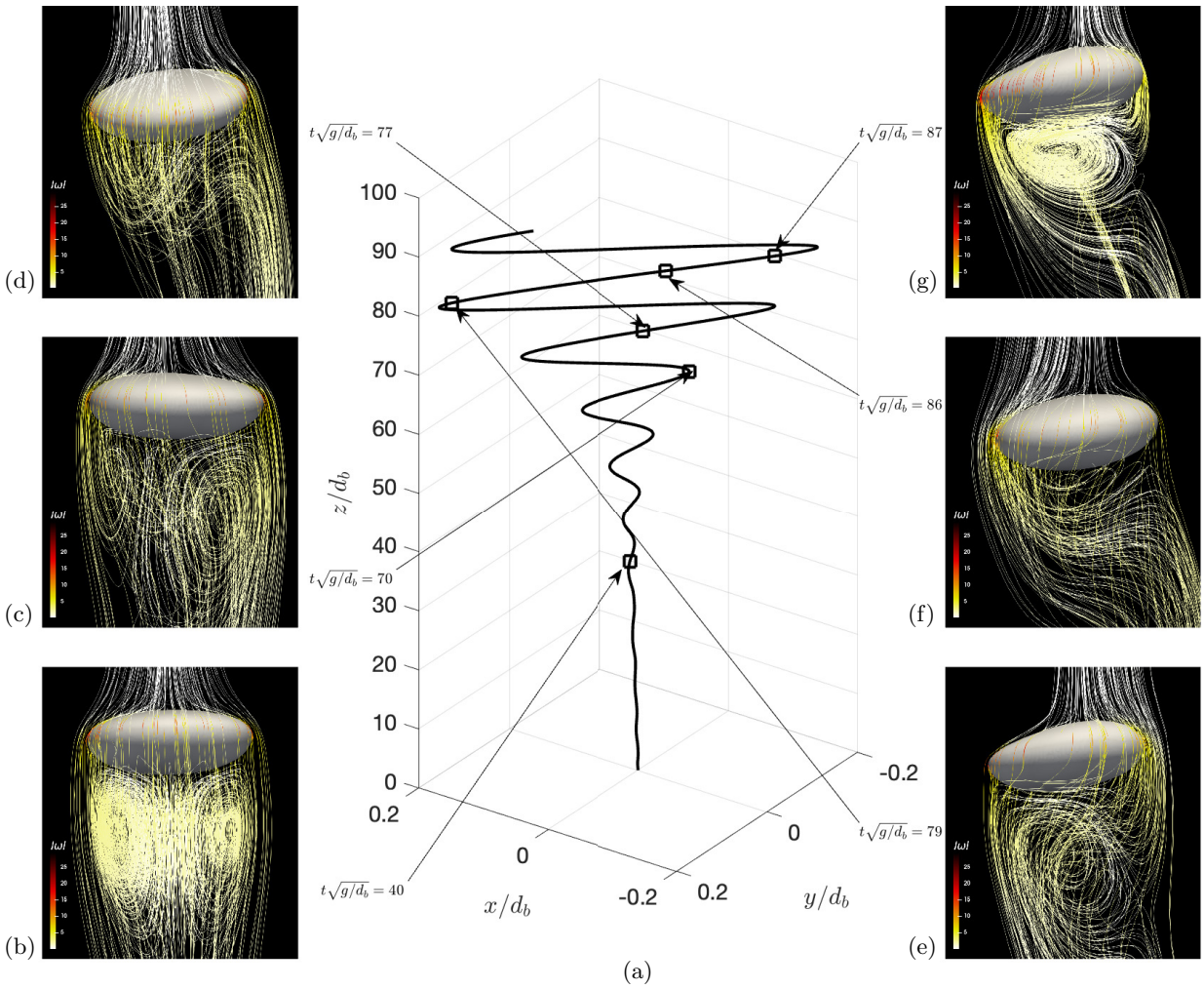

FIG. 11. Bubble trajectory and associated snapshots showing the bubble shape and surrounding flow for Ga = 100.25, Bo = 10; in the contaminated configuration Ma = 1. (a) Trajectory evolution, for $t\sqrt{g/d_b} = 0 - 90$. The streamlines calculated from the reference frame of the bubble are shown around the bubble in (b-g) at different time instants. The contaminated bubble follows a zig-zagging trajectory.

Figure 11(a) shows the bubble trajectory for the contaminated case, here increasing the Marangoni number to Ma = 1. Figures 11(b-g) show the streamlines and the bubble interface along the trajectory. When surfactant effects are introduced, we observe a transition in the trajectory from spiral to zigzag, together with a modification of the oscillation frequency. Similarly to the clean case, the bubble attains an oblate shape (b) with a recirculating wake forming behind the bubble before the oscillation starts. During these oscillations, the wake structure evolves with a recirculating cell appearing regularly (d, e, g) and a stronger intensity of wake phenomena than in the clean case (longer lived streamlines). The path is now characterized by zig-zag oscillations. During the zigzag oscillations the bubble oblateness is weaker as compared to the clean case.

We comment that contaminated bubbles deform less (i.e. remain more spherical) than clean bubbles, which we observe in both the axi-asymmetric and three-dimensional simulations. Magnaudet and Eames [102] explain this effect by the minimum pressure being higher on a contaminated bubble than on a clean bubble, related to the strength of rotational effects in the boundary layer, so that bubble deformation for a given set of parameters (Ga and Bo) is reduced.

We note that a similar transition from spiral to zigzag path has also been observed by Tagawa *et al.* [111] for experiments performed in water, with a higher Ga number (their experiment was conducted at Ga = 280 and Bo = 0.5) when they increased the surfactant concentration in the experiments. These comparisons suggest that surfactant effects at relatively high Ga and various Bo introduce a change in the path, from spiral to zigzag trajectories. That behavior might be relatively generic since it was observed using a linear isotherm in our numerical configuration

while the surfactants used in Tagawa *et al.* [111] are 1-Pentenol and Triton X-100.

The results call for a systematic three-dimensional study of the role of the Marangoni number on bubble trajectories for various range of Ga and Bo numbers, as well as a discussion on the role of the specific surfactant isotherm.

IV. CONCLUSION

The present study provides a numerical framework to simulate insoluble surfactant-laden 2D and 3D interfacial flows. We provide a hybrid method in which the momentum and surfactant transport equations, respectively, use the VoF and phase-field representation of the interface. The surfactant transport and Marangoni force calculation are tested against standard cases. The method conserves the mass of the surfactants and can be used with arbitrary interfacial isotherms or equations of state for the variation of surface tension. We also demonstrate that the method can handle surfactant transport with topological changes produced by the Plateau–Rayleigh instability. The implementation supports parallel computing and adaptive mesh refinement, is entirely open-source, and scripts are provided to reproduce the test cases and results. The surfactant transport equation in the present framework requires high resolution as the surface Péclet number increases and cannot be applied to strictly advective transport. Despite these limitations, the method can be applied to study various interfacial flows, such as drop and bubble dynamics, waves, or thin film motions.

Here, we apply the numerical framework to the case of surfactant-laden rising bubbles, considering an idealized linear isotherm. The strength of the surfactant effects is then determined by the Marangoni number, and the behavior when increasing the Marangoni number is akin to increasing the concentration of surfactants in experiments. We retrieve the qualitative and quantitative features of the effect of surfactants previously described in the literature, theoretically and experimentally. In the axisymmetric simulations, as the Marangoni number is increased, we observe the formation of a stagnant cap and immobilization of the interface, as well as the change of the bubble geometry to a more spherical shape at high Marangoni number. As a result, we observe and characterize the decrease of the terminal velocity as a function of Marangoni number. The slowing down of the rise velocity can be summarized in terms of the variation of the drag coefficient as a function of the stagnant cap angle and good agreement is observed when compared to the theoretical expression derived by Sadhal and Johnson [25] for creeping flow, even though our simulations are performed at relatively high Reynolds or Galileo numbers. This suggests that by parameterizing the dependence of the stagnant cap angle on the Marangoni number, a prediction for the drag coefficient of the bubble in the presence of surfactants for a wide range of conditions should be possible.

We also perform three-dimensional simulations of rising bubbles in the presence of surfactants. We consider conditions studied by Cano-Lozano *et al.* [107] of a bubble, with a clean interface, which follows a helicoidal trajectory. In the presence of surfactants, i.e., for a finite Marangoni number, we obtain a change in the bubble trajectory from helicoidal to zigzag. A similar change of trajectory was also reported in the experimental study by Tagawa *et al.* [111] made for higher Bond and Galileo numbers, when comparing clean and contaminated liquid. Further analysis of surfactants affecting the path instability is of great interest [110] and we believe the present open-source numerical framework will be beneficial to the community. Finally, the present computational framework could be used to explore the role of various surfactant isotherms and compare in detail against experimental work with measurements of specific surfactant isotherms, to quantitatively link the Marangoni number and the experimental conditions, as discussed and suggested in Erinin *et al.* [16] and Lohse [17].

ACKNOWLEDGMENTS

This work was supported by NSF grant 2242512 and NSF CAREER 1844932 to LD. The authors are pleased to acknowledge that the work reported on in this paper was substantially performed using the Princeton Research Computing resources at Princeton University which is a consortium of groups led by the Princeton Institute for Computational Science and Engineering (PICSciE) and the Office of Information Technology's Research Computing.

Declaration of Interests. The authors report no conflict of interest.

[1] M. J. Rosen and J. T. Kunjappu, *Surfactants and Interfacial Phenomena* (John Wiley & Sons, 2012).
[2] D. Myers, *Surfactant Science and Technology* (John Wiley & Sons, 2020).
[3] D. Lohse, Bubble puzzles: from fundamentals to applications, Physical Review Fluids **3**, 110504 (2018).
[4] D. Lohse, Fundamental fluid dynamics challenges in inkjet printing, Annual Review of Fluid Mechanics **54**, 349 (2022).

[5] L. Deike, Mass transfer at the ocean–atmosphere interface: The role of wave breaking, droplets, and bubbles, Annual Review of Fluid Mechanics **54**, 191 (2022).

[6] M. A. Bruning, M. Costalonga, S. Karpitschka, and J. H. Snoeijer, Delayed coalescence of surfactant containing sessile droplets, Physical Review Fluids **3**, 073605 (2018).

[7] E. Antonopoulou, O. Harlen, M. Rump, T. Segers, and M. Walkley, Effect of surfactants on jet break-up in drop-on-demand inkjet printing, Physics of Fluids **33** (2021).

[8] B. Néel and L. Deike, Collective bursting of free-surface bubbles, and the role of surface contamination, Journal of Fluid Mechanics **917**, A46 (2021).

[9] T. Bell, W. De Bruyn, C. A. Marandino, S. Miller, C. Law, M. Smith, and E. Saltzman, Dimethylsulfide gas transfer coefficients from algal blooms in the southern ocean, Atmospheric Chemistry and Physics **15**, 1783 (2015).

[10] B. Néel, M. Erinin, and L. Deike, Role of contamination in optimal droplet production by collective bubble bursting, Geophysical Research Letters **49**, e2021GL096740 (2022).

[11] J. Pierre, M. Poujol, and T. Séon, Influence of surfactant concentration on drop production by bubble bursting, Physical Review Fluids **7**, 073602 (2022).

[12] S. Poulain, E. Villermaux, and L. Bourouiba, Ageing and burst of surface bubbles, Journal of Fluid Mechanics **851**, 636 (2018).

[13] X. Liu and J. H. Duncan, The effects of surfactants on spilling breaking waves, Nature **421**, 520 (2003).

[14] X. Liu and J. H. Duncan, An experimental study of surfactant effects on spilling breakers, Journal of Fluid Mechanics **567**, 433 (2006).

[15] X. Liu and J. H. Duncan, Weakly breaking waves in the presence of surfactant micelles, Physical Review E **76**, 061201 (2007).

[16] M. Erinin, C. Liu, X. Liu, W. Mostert, L. Deike, and J. Duncan, The effects of surfactants on plunging breakers, Journal of Fluid Mechanics **972**, R5 (2023).

[17] D. Lohse, Surfactants on troubled waters, Journal of Fluid Mechanics **976**, F1 (2023).

[18] B. Franklin and W. Brownrigg, Xliv. of the stilling of waves by means of oil. extracted from sundry letters between benjamin franklin, LL. DFRS William Brownrigg, MDFRS and the Reverend Mr. Farish, Philosophical Transactions of the Royal Society of London , 445 (1774).

[19] A. Pockels, Surface tension, Nature **43**, 437 (1891).

[20] H. Manikantan and T. M. Squires, Surfactant dynamics: hidden variables controlling fluid flows, Journal of Fluid Mechanics **892**, P1 (2020).

[21] A. Frumkin, On surfactants and interfacial motion, Zhurnal Fizicheskoi Khimii **21**, 1183 (1947).

[22] V. G. Levich, *Physicochemical Hydrodynamics* (Prentice-Hall Inc., 1962).

[23] P. Savic, *Circulation and distortion of liquid drops falling through a viscous medium* (National Research Council Canada, 1953).

[24] R. Davis and A. Acrivos, The influence of surfactants on the creeping motion of bubbles, Chemical Engineering Science **21**, 681 (1966).

[25] S. Sadhal and R. E. Johnson, Stokes flow past bubbles and drops partially coated with thin films. part 1. stagnant cap of surfactant film–exact solution, Journal of Fluid Mechanics **126**, 237 (1983).

[26] J. Harper, The motion of bubbles and drops through liquids, Advances in Applied Mechanics **12**, 59 (1972).

[27] R. Bel Fdhila and P. Duineveld, The effect of surfactant on the rise of a spherical bubble at high Reynolds and Péclet numbers, Physics of Fluids **8**, 310 (1996).

[28] B. Cuenot, J. Magnaudet, and B. Spennato, The effects of slightly soluble surfactants on the flow around a spherical bubble, Journal of Fluid Mechanics **339**, 25 (1997).

[29] O. Atasi, B. Haut, A. Pedrono, B. Scheid, and D. Legendre, Influence of soluble surfactants and deformation on the dynamics of centered bubbles in cylindrical microchannels, Langmuir **34**, 10048 (2018).

[30] C. Pesci, A. Weiner, H. Marschall, and D. Bothe, Computational analysis of single rising bubbles influenced by soluble surfactant, Journal of Fluid Mechanics **856**, 709 (2018).

[31] M. Muradoglu and G. Tryggvason, Simulations of soluble surfactants in 3D multiphase flow, Journal of Computational Physics **274**, 737 (2014).

[32] O. Atasi, D. Legendre, B. Haut, R. Zenit, and B. Scheid, Lifetime of surface bubbles in surfactant solutions, Langmuir **36**, 7749 (2020).

[33] C. R. Constante-Amores, L. Kahouadji, A. Batchvarov, S. Shin, J. Chergui, D. Juric, and O. K. Matar, Dynamics of a surfactant-laden bubble bursting through an interface, Journal of Fluid Mechanics **911**, A57 (2021).

[34] M. O. Abu-Al-Saud, S. Popinet, and H. A. Tchelepi, A conservative and well-balanced surface tension model, Journal of Computational Physics **371**, 896 (2018).

[35] I. Seric, S. Afkhami, and L. Kondic, Direct numerical simulation of variable surface tension flows using a volume-of-fluid method, Journal of Computational Physics **352**, 615 (2018).

[36] M. K. Tripathi and K. C. Sahu, Motion of an air bubble under the action of thermocapillary and buoyancy forces, Computers & Fluids **177**, 58 (2018).

[37] G. Mialhe, S. Tanguy, L. Tranier, E.-R. Popescu, and D. Legendre, An extended model for the direct numerical simulation of droplet evaporation. Influence of the Marangoni convection on Leidenfrost droplet, Journal of Computational Physics **491**, 112366 (2023).

[38] H. A. Stone and L. G. Leal, The effects of surfactants on drop deformation and breakup, Journal of Fluid Mechanics **220**, 161 (1990).

[39] X. Li and C. Pozrikidis, The effect of surfactants on drop deformation and on the rheology of dilute emulsions in Stokes flow, Journal of Fluid Mechanics **341**, 165 (1997).

[40] S. Yon and C. Pozrikidis, A finite-volume/boundary-element method for flow past interfaces in the presence of surfactants, with application to shear flow past a viscous drop, Computers & fluids **27**, 879 (1998).

[41] Y. Jan and G. Trygvasson, Computational studies of contaminated bubbles, Symposium on Dynamics of Bubbles and Vortices Near a Free surface, ASME/AMD, 1991 **119**, 46 (1991).

[42] M. Muradoglu and G. Tryggvason, A front-tracking method for computation of interfacial flows with soluble surfactants, Journal of Computational Physics **227**, 2238 (2008).

[43] W. C. De Jesus, A. M. Roma, M. R. Pivello, M. M. Villar, and A. da Silveira-Neto, A 3d front-tracking approach for simulation of a two-phase fluid with insoluble surfactant, Journal of Computational Physics **281**, 403 (2015).

[44] G. Dziuk and C. M. Elliott, Finite elements on evolving surfaces, IMA Journal of Numerical Analysis **27**, 262 (2007).

[45] M. Lenz, S. F. Nemadjieu, and M. Rumpf, A convergent finite volume scheme for diffusion on evolving surfaces, SIAM Journal of Numerical Analysis **49**, 15 (2011).

[46] J.-J. Xu and H.-K. Zhao, An Eulerian formulation for solving partial differential equations along a moving interface, Journal of Scientific Computing **19**, 573 (2003).

[47] J.-J. Xu, Z. Li, J. Lowengrub, and H. Zhao, A level-set method for interfacial flows with surfactant, Journal of Computational Physics **212**, 590 (2006).

[48] P. Lakshmanan and P. Ehrhard, Marangoni effects caused by contaminants adsorbed on bubble surfaces, Journal of Fluid Mechanics **647**, 143 (2010).

[49] A. Piedfert, B. Lalanne, O. Masbernat, and F. Risso, Numerical simulations of a rising drop with shape oscillations in the presence of surfactants, Physical Review Fluids **3**, 103605 (2018).

[50] R. Van der Sman and S. Van der Graaf, Diffuse interface model of surfactant adsorption onto flat and droplet interfaces, Rheologica Acta **46**, 3 (2006).

[51] A. Yun, Y. Li, and J. Kim, A new phase-field model for a water–oil-surfactant system, Applied Mathematics and Computation **229**, 422 (2014).

[52] K. E. Teigen, X. Li, J. Lowengrub, F. Wang, and A. Voigt, A diffuse-interface approach for modeling transport, diffusion and adsorption/desorption of material quantities on a deformable interface, Communications in Mathematical Sciences **4**, 1009 (2009).

[53] K. E. Teigen, P. Song, J. Lowengrub, and A. Voigt, A diffuse-interface method for two-phase flows with soluble surfactants, Journal of Computational Physics **230**, 375 (2011).

[54] G. Soligo, A. Roccon, and A. Soldati, Coalescence of surfactant-laden drops by phase field method, Journal of Computational Physics **376**, 1292 (2019).

[55] K. Dieter-Kissling, H. Marschall, and D. Bothe, Direct numerical simulation of droplet formation processes under the influence of soluble surfactant mixtures, Computers & Fluids **113**, 93 (2015).

[56] J. G. Meijer, Y. Li, C. Diddens, and D. Lohse, Journal of Fluid Mechanics **966**, A14 (2023).

[57] T. Antritter, T. Josyula, T. Marić, D. Bothe, P. Hachmann, B. Buck, T. Gambaryan-Roisman, and P. Stephan, A two-field formulation for surfactant transport within the algebraic volume of fluid method, Computers & Fluids **275**, 106231 (2024).

[58] H. D. Ceniceros, The effects of surfactants on the formation and evolution of capillary waves, Physics of Fluids **15**, 245 (2003).

[59] S. Shin, J. Chergui, D. Juric, L. Kahouadji, O. K. Matar, and R. V. Craster, A hybrid interface tracking–level set technique for multiphase flow with soluble surfactant, Journal of Computational Physics **359**, 409 (2018).

[60] I. Cannon, G. Soligo, and M. E. Rosti, Morphology of clean and surfactant-laden droplets in homogeneous isotropic turbulence, Journal of Fluid Mechanics **987**, A31 (2024).

[61] K. Feigl, D. Megias-Alguacil, P. Fischer, and E. J. Windhab, Simulation and experiments of droplet deformation and orientation in simple shear flow with surfactants, Chemical Engineering Science **62**, 3242 (2007).

[62] Y. Y. Renardy, M. Renardy, and V. Cristini, A new volume-of-fluid formulation for surfactants and simulations of drop deformation under shear at a low viscosity ratio, European Journal of Mechanics-B/Fluids **21**, 49 (2002).

[63] A. J. James and J. Lowengrub, A surfactant-conserving volume-of-fluid method for interfacial flows with insoluble surfactant, Journal of Computational Physics **201**, 685 (2004).

[64] S. Popinet, Numerical models of surface tension, Annual Review of Fluid Mechanics **50**, 49 (2018).

[65] A. Rivière, W. Mostert, S. Perrard, and L. Deike, Sub-hinze scale bubble production in turbulent bubble break-up, Journal of Fluid Mechanics **917** (2021).

[66] L. Deike and W. K. Melville, Gas transfer by breaking waves, Geophysical Research Letters **45**, 10 (2018).

[67] W. Mostert, S. Popinet, and L. Deike, High-resolution direct simulation of deep water breaking waves: transition to turbulence, bubbles and droplets production, Journal of Fluid Mechanics **942**, A27 (2022).

[68] S. Popinet, An accurate adaptive solver for surface-tension-driven interfacial flows, Journal of Computational Physics **228**, 5838 (2009).

[69] S. S. Jain, A model for transport of interface-confined scalars and insoluble surfactants in two-phase flows, arXiv preprint arXiv:2311.11076 (2023).

[70] A. Limare, S. Popinet, C. Josserand, Z. Xue, and A. Ghigo, A hybrid level-set/embedded boundary method applied to solidification-melt problems, Journal of Computational Physics **474**, 111829 (2023).

[71] S. S. Jain, Accurate conservative phase-field method for simulation of two-phase flows, Journal of Computational Physics **469**, 111529 (2022).

[72] S. Popinet and collaborators, Basilisk, `http://basilisk.fr` (2013–2023).
[73] S. Popinet, A quadtree-adaptive multigrid solver for the serre–green–naghdi equations, Journal of Computational Physics **302**, 336 (2015).
[74] P. K. Farsoiya, Y. Mayya, and R. Dasgupta, Axisymmetric viscous interfacial oscillations–theory and simulations, Journal of Fluid Mechanics **826**, 797 (2017).
[75] P. K. Farsoiya, *Free and Forced, Linearised Interfacial Waves*, PhD Thesis, Indian Institute of Technology, Bombay (2019).
[76] A. Berny, L. Deike, T. Séon, and S. Popinet, Role of all jet drops in mass transfer from bursting bubbles, Physical Review Fluids **5**, 033605 (2020).
[77] P. K. Farsoiya, S. Popinet, and L. Deike, Bubble-mediated transfer of dilute gas in turbulence, Journal of Fluid Mechanics **920** (2021).
[78] P. K. Farsoiya, Q. Magdelaine, A. Antkowiak, S. Popinet, and L. Deike, Direct numerical simulations of bubble-mediated gas transfer and dissolution in quiescent and turbulent flows, Journal of Fluid Mechanics **954**, A29 (2023).
[79] P. K. Farsoiya, Z. Liu, A. Daiss, R. O. Fox, and L. Deike, Role of viscosity in turbulent drop break-up, Journal of Fluid Mechanics **972**, A11 (2023).
[80] G. Tryggvason, R. Scardovelli, and S. Zaleski, *Direct Numerical Simulations of Gas–Liquid Multiphase Flows* (Cambridge University Press, 2011).
[81] R. Scardovelli and S. Zaleski, Direct numerical simulation of free-surface and interfacial flow, Annual Review of Fluid Mechanics **31**, 567 (1999).
[82] J. U. Brackbill, D. B. Kothe, and C. Zemach, A continuum method for modeling surface tension, Journal of Computational Physics **100**, 335 (1992).
[83] L. E. Scriven, Dynamics of a fluid interface equation of motion for newtonian surface fluids, Chemical Engineering Science **12**, 98 (1960).
[84] H. A. Stone, A simple derivation of the time-dependent convective-diffusion equation for surfactant transport along a deforming interface, Physics of Fluids A: Fluid Dynamics **2**, 111 (1990).
[85] C. Min and F. Gibou, A second order accurate level set method on non-graded adaptive cartesian grids, Journal of Computational Physics **225**, 300 (2007).
[86] C. Min, On reinitializing level set functions, Journal of Computational Physics **229**, 2764 (2010).
[87] G. Russo and P. Smereka, A remark on computing distance functions, Journal of Computational Physics **163**, 51 (2000).
[88] S. S. Jain and A. Mani, A computational model for transport of immiscible scalars in two-phase flows, Journal of Computational Physics **476**, 111843 (2023).
[89] L. G. Leal, *Advanced transport phenomena: Fluid Mechanics and Convective Transport Processes*, Vol. 7 (Cambridge university press, 2007).
[90] N. Young, J. S. Goldstein, and M. Block, The motion of bubbles in a vertical temperature gradient, Journal of Fluid Mechanics **6**, 350 (1959).
[91] P. Farsoiya, H. A. Stone, S. Popinet, and L. Deike, Expanding Circle Test, `http://basilisk.dalembert.upmc.fr/sandbox/farsoiya/marangoni_surfactant/` (2024d).
[92] P. Farsoiya, H. A. Stone, S. Popinet, and L. Deike, Expanding Circle Test, `http://basilisk.dalembert.upmc.fr/sandbox/farsoiya/marangoni_surfactant/expanding_circle_test.c` (2024a).
[93] P. Farsoiya, H. A. Stone, S. Popinet, and L. Deike, Rotating Circle Test, `http://basilisk.dalembert.upmc.fr/sandbox/farsoiya/marangoni_surfactant/rotating_circle_test.c` (2024b).
[94] P. Farsoiya, H. A. Stone, S. Popinet, and L. Deike, Young et. al. Migrating Bubble Test, `http://basilisk.dalembert.upmc.fr/sandbox/farsoiya/marangoni_surfactant/young.c` (2024c).
[95] M. Herrmann, J. Lopez, P. Brady, and M. Raessi, Thermocapillary motion of deformable drops and bubbles, in *Proceedings of the Summer Program* (Stanford University, Center for Turbulence Research, 2008) p. 155.
[96] P. Farsoiya, H. A. Stone, S. Popinet, and L. Deike, Topological Test, `http://basilisk.dalembert.upmc.fr/sandbox/farsoiya/marangoni_surfactant/topological_test.c.c` (2024a).
[97] K. Kentheswaran, N. Dietrich, S. Tanguy, and B. Lalanne, Direct numerical simulation of gas-liquid mass transfer around a spherical contaminated bubble in the stagnant-cap regime, International Journal of Heat and Mass Transfer **198**, 123325 (2022).
[98] R. Clift, J. R. Grace, and M. E. Weber, *Bubbles, Drops, and Particles* (Courier Corporation, 2005).
[99] J. R. Grace, Shapes and velocities of single drops and bubbles moving freely through immisicible liquids, Transactions of the Institution of Chemical Engineers **54**, 167 (1976).
[100] W. Rybczynski, On the progressive motion of a liquid sphere in a viscous medium, Bulletin International de l'Academie des Sciences de Cracovie **1**, 40 (1911).
[101] R. Krishna and J. V. Baten, Simulating the motion of gas bubbles in a liquid, Nature **398**, 208 (1999).
[102] J. Magnaudet and I. Eames, The motion of high-reynolds-number bubbles in inhomogeneous flows, Annual Review of Fluid Mechanics **32**, 659 (2000).
[103] C. Ohl, A. Tijink, and A. Prosperetti, The added mass of an expanding bubble, Journal of Fluid Mechanics **482**, 271 (2003).
[104] A. Prosperetti, Bubbles, Physics of Fluids **16**, 1852 (2004).
[105] G. Mougin and J. Magnaudet, Path instability of a rising bubble, Physical Review Letters **88**, 014502 (2001).
[106] J. Tchoufag, J. Magnaudet, and D. Fabre, Linear instability of the path of a freely rising spheroidal bubble, Journal of Fluid Mechanics **751**, R4 (2014).

[107] J. C. Cano-Lozano, C. Martinez-Bazan, J. Magnaudet, and J. Tchoufag, Paths and wakes of deformable nearly spheroidal rising bubbles close to the transition to path instability, Physical Review Fluids **1**, 053604 (2016).
[108] P. Bonnefis, *Study of Wake, Shape and Trajectory Instabilities of Bubbles Using a Global Linear Stability Approach* , Ph.D. thesis, National Polytechnic Institute of Toulouse - INPT (2019).
[109] P. Bonnefis, J. Sierra-Ausin, D. Fabre, and J. Magnaudet, Path instability of deformable bubbles rising in newtonian liquids: A linear study, Journal of Fluid Mechanics **980**, A19 (2024).
[110] M. A. Herrada and J. G. Eggers, Path instability of an air bubble rising in water, Proceedings of the National Academy of Sciences **120**, e2216830120 (2023).
[111] Y. Tagawa, S. Takagi, and Y. Matsumoto, Surfactant effect on path instability of a rising bubble, Journal of Fluid Mechanics **738**, 124 (2014).
[112] K. Giribabu and P. Ghosh, Adsorption of nonionic surfactants at fluid–fluid interfaces: Importance in the coalescence of bubbles and drops, Chemical Engineering Science **62**, 3057 (2007).
[113] D. Kosior and J. Zawala, Initial degree of detaching bubble adsorption coverage and the kinetics of dynamic adsorption layer formation, Physical Chemistry Chemical Physics **20**, 2403 (2018).
[114] O. Atasi, M. Ravisankar, D. Legendre, and R. Zenit, Presence of surfactants controls the stability of bubble chains in carbonated drinks, Physical Review Fluids **8**, 053601 (2023).

Appendix A: Sensitivity of the terminal rise velocity with the grid size.

We verify the accuracy of the rise velocity of the axisymmetric bubble with respect to the grid size. Simulations at increasing levels of resolution, corresponding to an increasing number of grid points per bubble diameter are performed. Figure 12(a,b) shows the normalized rise velocities of the bubble for Ga $= 5, 100$, $Bo = 0.5$. Three different maximum level of refinement resolutions are used with adaptive mesh refinement, L9$\equiv$ $d_b/\Delta x = 25$, L10$\equiv$ $d_b/\Delta x = 50$, L11$\equiv$ $d_b/\Delta x = 100$. The velocity is grid converged for $Ga = 5$ between the resolution L9 and L10. As the Ga number is increased the resolution requirement increases (as the boundary layer is thinner). Fig. 12(b) shows the grid convergence for the highest Ga $= 100$, between L10 and L11. The maximum level of refinement L10 is therefore a resolution where all simulations show convergence in the terminal rise velocity. Such grid converged resolution is used for the analysis in the present study.

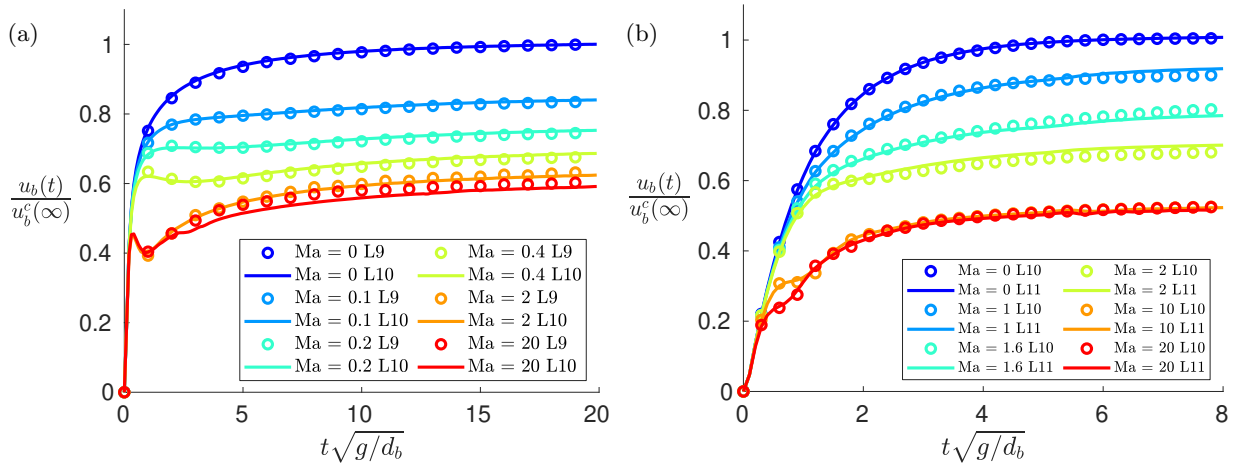

FIG. 12. Grid convergence for the rise velocity u_b, normalized by the terminal rise velocity of a clean bubble $u_b^c(\infty)$, for two sets of Ga, Bo numbers, and increasing Ma number. (a) Ga $= 5$, Bo $= 0.5$ (b) Ga $= 100$, Bo $= 0.5$. In each case circles indicate the lower resolution (in a, L9$\equiv$ $d_b/\Delta x = 25$; while in b L10$\equiv$ $d_b/\Delta x = 50$) and solid line indicates the higher resolution (a L10$\equiv$ $d_b/\Delta x = 50$, b L11$\equiv$ $d_b/\Delta x = 100$). The terminal rise velocity is grid independent in both cases. Similar conclusions are met with the other sets of parameters considered in the paper so that terminal rise velocity is grid converged at L10.